

Constraints on Compact Binary Formation and Effective Gravitational Wave Likelihood Approximation

A dissertation submitted in partial fulfillment of the
requirements
for the degree of Ph.D. *Doctor of Philosophy*
in Astrophysical Sciences and Technology
Vera Del Favero

School of Physics and Astronomy
Rochester Institute of Technology
Rochester, New York
August 25, 2022

ASTROPHYSICAL SCIENCES AND TECHNOLOGY
COLLEGE OF SCIENCE
ROCHESTER INSTITUTE OF TECHNOLOGY
ROCHESTER, NEW YORK

CERTIFICATE OF APPROVAL

Ph.D. DEGREE DISSERTATION

The Ph.D. Degree Dissertation of *Vera Del Favero* has been examined and approved by the dissertation committee as satisfactory for the dissertation requirement for the Ph.D. degree in Astrophysical Sciences and Technology.

Dr. Richard O'Shaughnessy, Dissertation Advisor

Dr. Ernest Fokoue, Committee Chair

Dr. Jason Nordhaus, Committee Member

Dr. Patricia Schmidt, Committee Member

Date _____

Constraints on Compact Binary
Formation and Effective
Gravitational Wave Likelihood
Approximation

By

Vera Del Favero

A dissertation submitted in partial fulfillment of the
requirements for the degree of Ph.D. in Astrophysical
Sciences and Technology, in the College of Science,
Rochester Institute of Technology.

August 25, 2022

Approved by

Dr. Andrew Robinson
Director, Astrophysical Sciences and Technology

Date

Declaration

I, VERA E. DEL FAVERO (“the Author”), declare that no part of this dissertation is substantially the same as any that has been submitted for a degree or diploma at the Rochester Institute of Technology or any other university. I further declare that the work in chapter 4 is entirely my own. Much of 3 consists of a review of the related literature, however the sections describing the properties of new population models are my own. Chapters 1, 2, and 5 draw in parts on work done with collaborators, including contributions from other authors. Those who have contributed scientific or other collaborative insights are fully credited in this dissertation, and all prior work upon which this dissertation builds is cited appropriately throughout the text.

Modified portions of this dissertation will be published by the author and her advisor, in a journal(s) yet to be determined.

- A substantial part of **Chapter 2** is based on the paper [63], entitled *Normal Approximate Likelihoods to Gravitational Wave Events*, authored by V. Delfavero, R. O’Shaughnessy, D. Wysocki, and A. Yelikar.
- The remainder of **Chapter 2** is based on the paper [64], entitled *Compressed Parametric and Non-Parametric Approximations to the Gravitational Wave Likelihood*, authored by V. Delfavero, R. O’Shaughnessy, D. Wysocki, and A. Yelikar.

Abstract

Since the initial discovery of gravitational-waves from merging black holes, the LIGO Scientific Collaboration together with Virgo and KAGRA have published 90 gravitational-wave observations of compact binary mergers in the Gravitational-Wave Transient Catalog papers. One of the quintessential questions of this decade in gravitational-wave astronomy is the characterization and impact of the population of observed gravitational-wave signals from merging black holes and neutron stars. Now, there is greater incentive than ever to study the formation channels for these compact binary mergers. In this work, we carry out an investigation of isolated binary evolution formation channel, comparing predictions of the gravitational-wave population from the StarTrack synthetic universe simulations to the observed population of compact binary mergers in order to constrain certain astrophysical processes in binary evolution. In due course, we construct, apply, and provide parametric and non-parametric models for the likelihood function of the full set of astrophysical parameters of each event in the Gravitational-Wave Transient Catalogs, including truncated multivariate normal distributions normalized on a bounded interval, which we have shared in our associated publications [63, 64]. We present the findings of our investigation of the formation parameters for the isolated binary evolution formation channel for compact objects. We have uncovered confounding systematic effects in our model by considering the agreement and disagreement of predictions based on the event rate and mass distribution. Furthermore, our preliminary results demonstrate the benefits of a multi-dimensional analysis which is sensitive to the interdependence of the predicted detection population on many formation parameters. Our essential contribution is therefore a method for carrying out such an analysis efficiently, while considering its self-consistency. We discuss potential sources of bias as we also present the properties of our best binary evolution models, which are consistent with unrestricted stellar mass loss due to winds, high mass and angular momentum loss to ejected portions of a common envelope, and substantial black hole supernova recoil kicks. We conclude with a discussion of the impact of these activities for gravitational-wave and multi-messenger astronomy.

Contents

| | | |
|----------|---|-----------|
| 1 | Introduction | 3 |
| 1.1 | Characterizing Gravitational-Wave Observations | 4 |
| 1.2 | Origins of Compact Binary Objects | 6 |
| 1.3 | Organization of this Dissertation | 6 |
| 2 | Normal Approximate Likelihoods for Gravitational Wave Events | 8 |
| 2.1 | Constructing the Likelihood from PE Samples | 10 |
| 2.1.1 | Gaussian Process Marginal Densities | 11 |
| 2.2 | Normal Approximate Likelihood Modeling | 12 |
| 2.2.1 | The NAL Model Parameters | 13 |
| 2.2.2 | NAL Optimization | 13 |
| 2.3 | Properties of NAL Models for GWTC Events | 15 |
| 2.3.1 | Aligned Spin | 16 |
| 2.3.2 | Precessing spin models | 19 |
| 2.3.3 | Tidal Parameters | 19 |
| 2.4 | Applications of NAL Models | 20 |
| 2.4.1 | Properties of the Gravitational-Wave Population | 22 |
| 2.4.2 | Applications for Low-Latency Parameter Estimation | 23 |
| 3 | Simulating the Evolution of Massive Binary Star Systems | 26 |
| 3.1 | The Evolution of Massive Stars and Binaries | 26 |
| 3.1.1 | Supernova Engines | 27 |
| 3.1.2 | Interacting Binaries and the Common Envelope Phase | 29 |
| 3.2 | Simulating Populations of Massive Binaries with StarTrack | 30 |
| 3.2.1 | Initial Mass Function | 31 |
| 3.2.2 | Single Star Evolution Assumptions | 32 |
| 3.2.3 | Binary Evolution | 33 |
| 3.3 | Cosmological Postprocessing | 33 |
| 3.3.1 | Estimating a Merger Rate | 34 |
| 3.3.2 | Predicting the Gravitational-Wave Detection Rates | 35 |
| 3.4 | Simulation Properties | 36 |
| 3.4.1 | Initial Models | 36 |

| | | |
|----------|--|-----------|
| 3.4.2 | Preliminary Uniform Parameter Space | 39 |
| 3.4.3 | Delayed Supernova Engine and Wind | 41 |
| 4 | Population Synthesis | 42 |
| 4.1 | Bayesian Population Inference | 42 |
| 4.1.1 | Detection Rate Likelihood | 43 |
| 4.1.2 | Shape Likelihood | 44 |
| 4.1.3 | Joint Likelihood | 44 |
| 4.2 | Kick Velocity; A One-Dimensional Study | 45 |
| 4.3 | Higher-Dimensional Studies: $f_a, \beta, \sigma_{\text{kick}}, f_{\text{wind1}}$ | 45 |
| 4.3.1 | The Delayed Supernova Engine | 46 |
| 4.3.2 | Constraints on Isolated Binary Evolution in Four Dimensions . . | 48 |
| 5 | Conclusions | 51 |
| 5.1 | Summary | 51 |
| 5.2 | Broader Impacts of Science and Methodology | 52 |

Chapter 1

Introduction

On September 14th, 2015, the first gravitational-wave signal from a coalescing binary-black-hole was detected by the Laser Interferometer Gravitational-Wave Observatory (LIGO), and reported by the LIGO Scientific Collaboration (LSC) [3, 10, 2]. Now, after the third observing run of LIGO together with Virgo and KAGRA (KAmioka GRAvitational-wave detector), astronomers have reported a variety of compact binary merger events, including Binary Black-Hole (BBH), Binary Neutron-Star (BNS), and Neutron-Star Black-Hole (NSBH) systems. [8, 13, 18]. These observations have been summarized by many groups including the ninety events reported in the Gravitational-Wave Transient Catalogs (GWTCs) as well as independent analysis [4, 9, 50, 52, 98, 142, 35, 108, 42]. In the era of multi-messenger astronomy, these and future gravitational-wave observations describe a view of the cosmos set by more than just electromagnetic radiation.

Each gravitational-wave signal is a strain imposed on the interferometer instruments. These signals are identified by a rapid search, and events which may have electromagnetic counterparts are immediately constrained by a low-latency parameter estimation pipeline [1, 178, 61]. Following this, all events are then characterized by robust Bayesian statistical inference in gravitational-wave parameter estimation (PE) [155, 196, 31, 125, 17, 98]. Such an inference evaluates the agreement between strain information and relativistic waveform models, to yield accurate parameter estimates for each detection.

Once the properties of individual gravitational-wave sources are characterized, a question which arises as to how these systems form in The Universe. The formation of these compact binary objects can be described by a variety of channels, one of which is the formation of massive stellar binaries by isolated evolution [140, 26, 27, 28, 39]. The properties of every individual gravitational-wave event can be incorporated into a model of the compact binary merger population, which has implications for the astrophysical significance of these formation channels [6, 188, 51, 207, 208].

In this dissertation, I demonstrate an efficient characterization of the properties of

the gravitational-wave observations in the Gravitational-Wave Transient Catalogs, in order to constrain the processes by which massive stellar binaries evolve to become merging compact binaries. This work builds upon my existing publications [63, 64]. We make use of the StarTrack code to evaluate constraints on binary evolution using simulated populations of merging binaries.

1.1 Characterizing Gravitational-Wave Observations

Models describing a gravitational-wave signal are characterized by some parameters, λ , consisting of some *extrinsic* parameters representing the sky location, distance, and the orientation of the system, as well as *intrinsic* parameters which fully characterize the astrophysical properties of an event without reference to the observer. The intrinsic parameters we study in our work are the mass (m_i , in units of solar mass, M_\odot), dimensionless spin (χ_i), and tidal deformability of neutron stars (Λ_1, Λ_2). The *astrophysical* parameters include the intrinsic parameters as well as luminosity distance (l , in units of Mpc), as the age of the Universe at the time of merger is a quantity of astrophysical interest.

Additional parameterizations are useful for more precisely measuring the properties of a gravitational-wave observation, due to the sensitivity of the waveform, a desire for Gaussian uncertainty, and coordinate degeneracies. These parameters include the total mass $M = m_1 + m_2$, the symmetric mass ratio $\eta = (m_1 m_2) M^{-2}$, the chirp mass $\mathcal{M}_c = \eta^{3/5} M^{2/5}$, and inverse luminosity distance l^{-1} . Except where specified, mass parameters are characterized in the source-frame. The relationship between source-frame and detector-frame mass parameters depends on cosmological redshift: $M_z = M_s(z + 1)$. We make use of the standard effective spin parameter which is aligned with the orbital angular momentum of the system, \mathbf{L} [60, 164, 14]:

$$\chi_{\text{eff}} = (\chi_1 m_1 + \chi_2 m_2) \cdot \hat{\mathbf{L}} / M \quad (1.1)$$

We make use of the standard Cartesian coordinate system defined such that \hat{z} is orthogonal to the plane of the orbit at the reference time (frequency) at which orbital initial data is specified (i.e. $\hat{z} = \hat{L}$).

The likelihood $\mathcal{L}(h(\lambda)) \equiv \mathcal{L}(\lambda)$ of a known gravitational-wave signal $h(t|\lambda)$ can be evaluated in a parameter space, λ , based on some knowledge of the detector noise. Detailed models for gravitational-wave emission provide estimates for $h(t|\lambda)$ [155, 196, 31, 125, 17, 98, 2]. The Bayesian problem of gravitational-wave parameter inference is to characterize the posterior probability of each event as a function of its parameters [23]. This requires a careful and thorough investigation of the prior information characterized by a fiducial prior, $p(\lambda)$. The posterior probability is therefore proportional to $\mathcal{L}(\lambda)p(\lambda)$.

Many groups are working on characterizing each event using full numerical relativity [93, 2, 166, 19, 94, 137, 130, 211, 101, 35, 108, 42]. While a full numerical

relativity approach is necessary to simulate precessing compact binaries during inspiral and merger in complete rigor, many groups including the LSC use approximants which can be evaluated more quickly on the scale required for parameter estimation. These approximants include IMRPhenomD [102, 112], IMRPhenomPv2 [91, 111], IMRPhenomPv3 [113], IMRPhenomPv3HM [149], IMRPhenomXPHM [163, 82, 162], SEOBNRv3 [154, 183], SEOBNRv4 [33], SEOBNRv4PHM [57, 150], and NRSur7dq4 [195], as well as others [138, 138, 65, 66, 95, 180].

One such parameter estimation framework developed by my colleagues at RIT is the Rapid parameter inference on gravitational-wave sources via Iterative FiTing (RIFT) algorithm, which addresses the challenge of iteratively fitting the posterior probability for gravitational-wave sources in some set of parameters [125]. This is accomplished by choosing points in that parameter space and evaluating an expensive likelihood function for the waveform best characterizing a given signal. Those likelihood evaluations are then interpolated and weighted by the fiducial prior, in order to reconstruct the posterior probability function, in the form of a large set of samples (λ_k) representing fair draws which fully characterize that posterior.

Several key science objectives of gravitational-wave astronomy explore the astrophysical implications of the entire population of observed compact binary mergers. These *population synthesis* calculations are often Monte Carlo simulations of millions of synthetic merging binaries. To assess the net likelihood of a specific population synthesis model therefore often requires large scale Monte Carlo integrals of the likelihood of each gravitational-wave event [182, 208, 51, 28, 37, 171, 71, 189, 196, 17]. As the sensitivity of the detectors increases towards design sensitivity in the coming years, these calculations will become more and more computationally expensive as the population of gravitational-wave events grows [76]. For other applications, an evaluation of $\mathcal{L}(\lambda)$ is required, which sample-based methods may fail to provide.

There are many methods for reconstructing this likelihood function, including sample-based methods such as Kernel Density Estimates (KDEs) and histograms [84]. Such sample-based methods are useful for low-dimensional models, but often scale poorly to higher-dimensional use cases, requiring an increasing number of samples to fully characterize the intrinsic parameters of an event. Carefully tuned non-parametric methods can protect models from binning and smoothing effects (for example, see [86] with the binary neutron star merger, GW170817). Compressed parametric models, such as the multivariate normal distribution pose a viable alternative to sample-based methods [46, 2, 125, 109]. Fast and accurate approximations for the likelihood function $\mathcal{L}(\lambda)$ are essential to carrying out the central calculation of a population synthesis algorithm.

The multivariate normal distribution has long been used to describe the likelihood of gravitational-wave events in coordinates well suited to waveform models. However, a truncated set of samples can introduce bias in a sample-based parameterization of the multivariate normal distribution [63, 64]. In our previous work, we have introduced bounded multivariate Normal Approximate Likelihood (NAL) models for each event, which fully characterize the precessing degrees of freedom of each gravitational-wave event in the GWTCs [63, 64]. These models overcome bias introduced by finite bound-

ary effects and are efficient in both generating samples and evaluating a likelihood estimate. They lend themselves immediately to both population work and low-latency gravitational-wave parameter estimation.

1.2 Origins of Compact Binary Objects

Theories of how compact binary objects form include dynamic mergers in a dense stellar cluster, as well as the binary evolution of massive stars, with some mechanism for ejecting orbital angular momentum from the system [25, 177, 83, 21, 134, 213, 212, 145, 120, 139, 15, 16, 136]. With some noteworthy exceptions, such as the BNS observation, GW170817, gravitational-wave detections often are not accompanied by an electromagnetic counterpart [5, 58, 59, 114, 175, 110]. Most often, we must infer the astrophysical origin of compact binary sources from the gravitational-wave signal alone. Many studies have shown that isolated binary evolution can produce most of the events published thus far in the GWTCs [140, 26, 27, 29, 28, 39, 75]. Exceptions to this would include events with a high orbital eccentricity and precessing spin components, such as proposed for events like GW190521 in the third LIGO observing run [83, 188, 51]. In the remainder of this work, we focus on the isolated binary evolution formation channel for compact binary objects.

As most compact binary objects are expected to originate from isolated binary evolution, the population of gravitational-wave signals detected so far allow us to constrain the bulk properties of this binary evolution formation channel. This is accomplished by comparing the real gravitational-wave observations from published catalogs to predicted populations of compact binary mergers, with different assumptions about binary evolution using a Bayesian inference framework [23]. In our work, we use the NAL models for the likelihood of each event in the Gravitational-Wave Transient Catalogs to carry out this inference. We incorporate these models together with the StarTrack population synthesis code for the prediction of compact binary mergers from isolated binary evolution and an associated cosmological postprocessing setup [67, 68, 69, 28].

1.3 Organization of this Dissertation

In chapter 2 I describe the Normal Approximate Likelihood (NAL) models for the likelihood of gravitational-wave events introduced in Delfavero et al. (2021 and 2022) [63, 64]. Chapter 3 reviews some of the pertinent background and literature for the isolated binary evolution models we constrain as well as the formulation for predicting the gravitational-wave detection rate for simulated synthetic universes with the StarTrack code. Following this, chapter 4 demonstrates the Bayesian framework used to constrain these processes by comparing individual simulations with different sets of formation parameters. Finally, chapter 5 discusses the astrophysical implications of our research.

This dissertation summarizes the work in two of my previous papers, including Delfavero et al. (2021) [63] and Delfavero et al. (2022) [64]. I have made contributions to RIFT in the past, such as in my master’s thesis [62]. While I continue to contribute to parameter estimation efforts, such as in the forthcoming paper by Wofford et al. (2022) [204], these are not the focus of this dissertation. My contributions to efforts to constrain the neutron star equation of state are also not the focus of this dissertation [97], although this work will be discussed briefly as an example of the astrophysical consequences of our population synthesis.

Chapter 2

Normal Approximate Likelihoods for Gravitational Wave Events

As described in section 1.1, each gravitational-wave signal detected by an observatory connected to LVK is observed as a strain incident on the detector [8, 3]. In order to characterize the properties of each event, parameter estimation groups use Bayesian inference, and compare this strain information to relativistic waveform models described by a set of parameters (including the astrophysical parameters λ) [155, 196, 125, 17, 98, 23]. In publications such as the Gravitational-Wave Transient Catalogs, these parameter estimates are released as a set of identically distributed independent random samples from the posterior of each event, as well as single-valued parameter estimates which provide single-parameter credible intervals (i.e., from their one-dimensional marginal distributions) [4, 9, 52, 50, 98, 142, 35, 108, 42, 48, 49]. In this work we focus on GWTC events, however these methods can be applied to any sample-based estimate for the parameters of an arbitrary probability distribution.

In low dimensionality sample-based estimates of the likelihood function, such as a Kernel Density Estimate (KDE), can provide an accurate representation of the likelihood function for a gravitational-wave event [63, 84]. These sample-based estimates reconstruct the likelihood by re-weighting posterior samples by the inverse prior (see section 2.1). These methods are ultimately limited in higher-dimensional parameter spaces by the number of samples required to construct an accurate approximation, which increases with dimensionality. Therefore, as sample-based methods such as this are restricted to the parameter estimation samples released with each catalog, and the computational cost of these sample-based estimates increases with the number of samples, these methods are not suitable to large-scale population inference.

As adopting a likelihood function from these samples can be non-trivial, and as the sample mean often fails to describe the Maximum Likelihood Estimate (MLE) for the parameters of each gravitational wave event, we explore alternative representations of the same parameter estimation samples through bounded (truncated) Normal Approximate

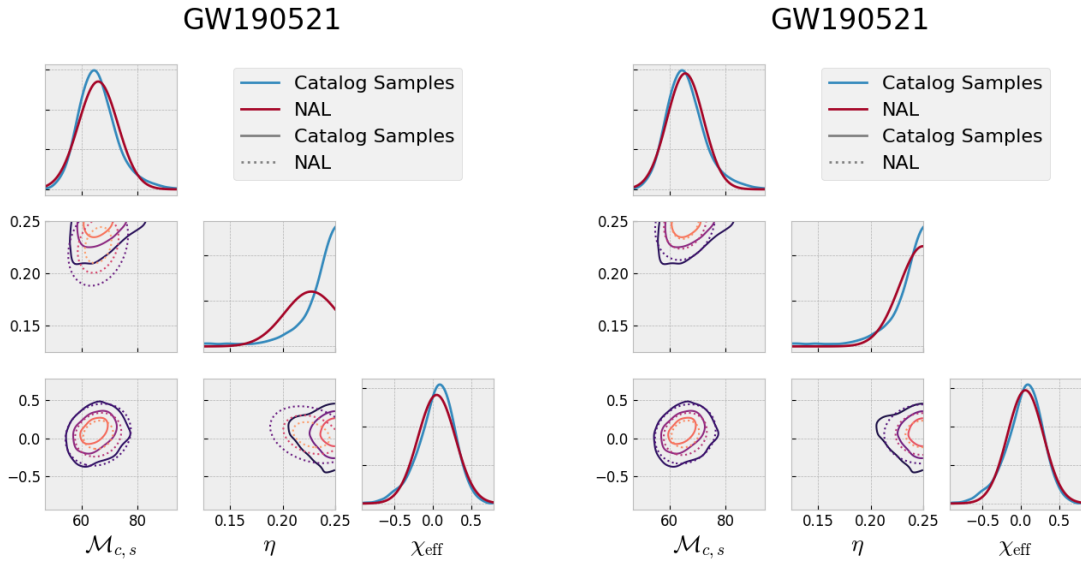


Figure 2.1: NAL models for GW190521 (<https://dcc.ligo.org/public/0169/P2000223/007/GW190521.tar> - using the ‘PublicationSamples’ set of samples), using *implicit* (left) and *optimized* (right) fit parameters. These corner plots evaluate the inferred likelihood function in one (diagonal) and two (off-diagonal) sample spaces. In the one-dimensional spaces, the blue curve indicates a non-parametric estimate of published samples, while the red curve indicates the properly re-normalized Gaussian. In the two-dimensional sample spaces, contours are drawn enclosing [25, 50, 75] percent of the likelihood. Note that optimized NAL models overcome the boundary effect present for the implicit fit near equal mass ($\eta = 0.25$). The one- and two-dimensional sample estimates which are compared to each Gaussian are the marginal density estimates described in section 2.1.1

mate Likelihood (NAL) models [63, 64]. These models overcome limitations imposed by a finite set of samples, to provide computationally efficient likelihood approximations which are not restricted by the same finite boundary effects as non-truncated Gaussians (consider samples of the symmetric mass ratio for an equal mass event, e.g. fig 2.1). The parameters of each NAL model also describe a less biased MLE description of the astrophysical properties of each event.

In this chapter, I will describe my methods for using data products such as the GWTC parameter estimation samples to approximate the likelihood function for each published gravitational-wave event in its full set of astrophysical parameters. I will also describe the immediate astrophysical consequences following the NAL models, such as the properties of our gravitational-wave population. Finally, I will discuss several potential applications of these methods. The work in this chapter relies heavily on the associated papers [63, 64].

2.1 Constructing the Likelihood from PE Samples

When using samples to construct a general parametric model for some density, it is useful to first construct a non-parametric model which is accurate (even if comparatively more expensive to evaluate). Following this, one can generate a set of evaluations to compare with the parametric model. This section highlights the non-parametric Gaussian Process (GP) models for the one- and two-dimensional marginalization of each set of parameters. These GP models are fully generic, not assuming Gaussian behavior, providing efficient and accurate approximations to the sample density, and which may themselves be desired for additional applications.

Reconstructing a likelihood density from the posterior samples first requires re-weighting samples by the inverse prior [23, 125]. The GWTC releases use an uninformed prior which is uniform in detector-frame component masses and spin magnitude and direction [43]. Alternatively, in terms of $\mathcal{M}_{c,z}$ (detector-frame chirp mass) and η :

$$p(\mathcal{M}_{c,z}, \eta) d\mathcal{M}_{c,z} d\eta = \frac{4}{(M_{\max} - m_{\min})^2} \frac{\mathcal{M}_{c,z} d\mathcal{M}_{c,z} d\eta}{\eta^{6/5} \sqrt{1 - 4\eta}} \quad (2.1)$$

where we have for simplicity adopted prior boundaries in $\mathcal{M}_{c,z}$ and η so the distribution takes a simple product form. When applicable, the distance prior we remove is the square of the inverse luminosity distance $1/l^2$. Our method is not limited to an uninformed prior, and the same methods could be applied for posterior samples drawn with an informed prior [198].

There are various methods for providing a sample-based estimate of the likelihood function. In low dimensionality, a KDE provides an accurate estimate of the likelihood function for a gravitational-wave, and we use KDEs in our first paper, as the intermediate approximation to the likelihood [63, 84]. However, the evaluation of a KDE for a given point in parameter space requires a high computational cost, as the evaluation

scales with the number of samples used for the estimate. Some events in LIGO’s third observing run have $> 10^5$ samples, which make KDEs less than ideal [9].

Histograms provide a simple sample-based method but require smoothing and careful handling to avoid overfitting or underfitting samples. Others have done a lot of work developing adaptive binning algorithms for flexible histograms which try to avoid these errors by using different bin widths throughout a sample [173]. Some of these methods are used in gravitational-wave likelihood estimation [55, 210, 56, 126]. These methods are well tested in one dimension, are computationally limited in higher dimensions. Some of these methods are still prone to overfitting.

In order to recover the marginal likelihood for our parameters in one and two dimensions, we rely on histograms with a fixed bin width optimized by minimizing binning effects. We smooth these histograms using a Gaussian Process, and we share our methods below:

2.1.1 Gaussian Process Marginal Densities

Gaussian Process Regression is a non-parametric method of approximating the value of a function in a given parameter space, given some sample function values (“training data”) [201]. GP methods use a kernel, or a set of basis functions which describe the covariance of points in the space explored by the model. The function value at each point in the space described by a Gaussian Process can be described by a multivariate normal random variable. These methods can be reliable, and are useful in statistical inference due to their ability to make predictions directly by providing a mean and covariance for the estimated value of a given function.

GP methods are known to be highly accurate while also being computationally expensive, where the time required to evaluate the function on a sample scales with the cube of the number of training points provided in traditional methods. This cost can be mitigated by selecting a kernel that enables sparse matrix operations, allowing the evaluation of the GP on a given sample to consider only the points closest to that sample. Williams and Rasmussen provide such a kernel in the form of the piecewise polynomial kernel with compact support [201]. Together with compiled evaluations of the basis functions themselves, the computational cost can be reduced by several orders of magnitude compared to sci-kit learn [156]. Our Gaussian Process code is available at

<https://gitlab.com/xevra/gaussian-process-api>. This package performs a Gaussian Process fit in an arbitrary number of dimensions using compiled sparse-matrix kernel operations and sparse Cholesky matrix inversion. Our package also provides a whitenoise kernel, necessary for many applications.

In addition to the Gaussian Process Regression interpolator, the package provides a way to construct an estimate to a weighted sample density function, as a set of one- and two-dimensional marginal density estimates, or as an k-dimensional density estimate. The k-dimensional estimate is not required for our applications, and requires additional testing, so we leave it out of this discussion.

Our method for reconstructing the one- and two- dimensional likelihood from re-weighted posterior samples begins with a histogram with some number of bins, n . We consider the centers of each bin our training inputs, X_n , and our normalized histogram values make up our training values Y_n . A Gaussian Process is used to smooth histogram values, and is labeled $f_n(\lambda)$, using standard binomial error estimates. We then construct a similar histogram and Gaussian Process $f_{n+1}(\lambda)$, using $n + 1$ bins. For two- and higher-dimensional histograms, all bins are incremented together - but need not be identical. We cross-evaluate our models to further estimate the error of each model, which is summed in quadrature with binomial error estimates.

$$\delta Y_n = |Y_n - f_{n+1}(X_n)| \quad (2.2)$$

$$\delta Y_{n+1} = |Y_{n+1} - f_n(X_{n+1})| \quad (2.3)$$

By incrementing the number of bins, we choose n to minimize these error estimates, using a Kolmogorov-Smirnov test [121]. The Kolmogorov-Smirnov test measures the maximum value of the difference between two distributions. We refrain from using a more sophisticated measure of the difference between two distributions in order to avoid over-complicating a new method. In the future, a different test may be used.

One limitation of this method without any additional work is that the training data (X_n) are placed at the centers of histogram bins. Therefore, there will be no training points in the outermost half-bin-width region of the histogram. If we use $f_n(X)$ to estimate the value of the likelihood function in that outermost half-bin-width region, we are required to extrapolate rather than interpolate. This is more difficult to accomplish accurately with a Gaussian Process not designed specifically for extrapolation.

We can overcome this limitation by imposing a boundary condition on our histogram, taking advantage of the fact that histograms estimate a probability distribution only in a bounded region. This boundary condition effectively mirrors the sample about the boundary in only a half-bin-width region outside the histogram limits. Extending the influence of the histogram by one half-bin-width allows the outer-most bins for our histogram to lie precisely on the boundary. This allows us to avoid extrapolating with our Gaussian Process. Finally, we construct an additional Gaussian Process, $g(\lambda)$, which is trained using the combined training sets and estimated errors for $f_n(\lambda)$ and $f_{n+1}(\lambda)$, with our final choice of n . We find that $g(\lambda)$ offers a more informed Gaussian Process than those generated by individual histograms.

2.2 Normal Approximate Likelihood Modeling

The multivariate normal distribution is a standard tool for effective approximations for the gravitational-wave likelihood function in suitable coordinates [2, 158, 146, 45, 147]. Multivariate normal models have many desirable properties, including fast density eval-

uation and ease of generating random samples. However, a normal approximation does not arise naturally in generic coordinates, but only when using a parameterization well suited to the signal, such that the coordinates chosen are expected to be dominated by Gaussian noise. Unfortunately, many of these desired coordinates are limited by a finite domain (see fig 2.1). In cases where the likelihood appears Gaussian-like with significant truncation, an optimized bounded multivariate normal distribution will preserve the desired properties of a Gaussian model and better represent a sample density than simply assuming the sample mean and covariance for the parameters of a Gaussian. This section summarizes the parameters and optimization process for the Normal Approximate Likelihood (NAL) model.

2.2.1 The NAL Model Parameters

A generalized multivariate normal distribution can be characterized fully by the location of its peak (μ) and a covariance matrix (Σ).

$$G(\lambda - \mu, \Sigma) = (|2\pi\Sigma|)^{-\frac{1}{2}} \exp \left[-\frac{1}{2}(\lambda - \mu)^T \Sigma^{-1}(\lambda - \mu) \right] \quad (2.4)$$

The NAL parameterization of these quantities includes a decomposition of Σ into the characteristic standard deviation parameters, σ , and the correlation matrix, ρ , where $\Sigma = \sigma\rho\sigma^T$. This decomposition is especially effective because the correlation parameters have useful properties, including symmetry ($\rho_{i,j} = \rho_{j,i}$), unity along the diagonal ($\rho_{i,i} = 1$), and bounds ($-1 \leq \rho_{i,j} \leq 1$). The expression for a k -dimensional space expands to:

$$\begin{pmatrix} \sigma_1^2 & \sigma_1\sigma_2\rho_{1,2} & \cdots & \sigma_1\sigma_k\rho_{1,k} \\ \sigma_1\sigma_2\rho_{1,2} & \sigma_2^2 & \cdots & \sigma_2\sigma_k\rho_{2,k} \\ \vdots & \vdots & \ddots & \vdots \\ \sigma_1\sigma_k\rho_{1,k} & \sigma_2\sigma_k\rho_{2,k} & \cdots & \sigma_k^2 \end{pmatrix} = \begin{pmatrix} \sigma_1 \\ \sigma_2 \\ \vdots \\ \sigma_k \end{pmatrix} \begin{pmatrix} 1 & \rho_{1,2} & \cdots & \rho_{1,k} \\ \rho_{1,2} & 1 & \cdots & \rho_{2,k} \\ \vdots & \vdots & \ddots & \vdots \\ \rho_{1,k} & \rho_{2,k} & \cdots & 1 \end{pmatrix} \begin{pmatrix} \sigma_1 \\ \sigma_2 \\ \vdots \\ \sigma_k \end{pmatrix}^T \quad (2.5)$$

where, $(k^2 + 3k)/2$ parameters must be optimized (e.g. a three-dimensional model will have nine parameters, while an eleven-dimensional model will have seventy-seven parameters).

2.2.2 NAL Optimization

As one- and two-dimensional marginals fully capture the behavior of a generalized bounded multivariate normal distribution, we can optimize a high-dimensional NAL model by evaluating the goodness of fit using one- and two-dimensional marginalization.

A one-dimensional marginal in the i 'th dimension is fully characterized by μ_i and σ_i , as $G_i(\lambda_i) = G(\lambda_i - \mu_i, \sigma_i)$. Similarly, a two-dimensional marginal in the i 'th and j 'th components is fully characterized by $\mu_i, \mu_j, \sigma_i, \sigma_j$, and ρ_{ij} , as $G_{i,j}(\lambda_{i,j}) = G([X_i, X_j] - [\mu_i, \mu_j], [[\sigma_i^2, \sigma_i\sigma_j\rho_{ij}], [\sigma_i\sigma_j\rho_{ij}, \sigma_j^2]])$. By evaluating $G_i(\lambda_i)$ and $G_{i,j}(\lambda_{i,j})$ in a bounded region, and normalizing in that bounded region, one can invoke a standard convergence test to evaluate the goodness of fit between a set of Gaussian parameters and an estimate of the sample density.

In our procedure, we use the **Kullback-Leibler (KL) divergence** to evaluate the agreement of our NAL models with the Gaussian Process sample density estimates outlined previously (sec 2.1.1). The KL divergence measures the ability of a secondary probability distribution ($Q(x)$) to describe a primary probability distribution ($P(x)$), and is given by:

$$D_{\text{KL}}(P|Q) = \sum_{x \in \mathbf{x}} P(x) \log \left(\frac{P(x)}{Q(x)} \right) \quad (2.6)$$

It also represents the information lost by approximating $P(x)$ with $Q(x)$. The KL divergence is sensitive to logarithmic differences between P and Q . The quantity is well suited to our purposes, as we compare a wide variety of guesses (as secondary distributions) to fixed (primary) one and two-dimensional marginal sample distributions during optimization. The quality of a particular guess in the optimization is described by the mean of the one- and two-dimensional KL divergences which describe the one- and two-dimensional marginals of the NAL model.

Initially, we explored various packaged optimization routines, such as Newton's method and Emcee [74]. We found that these optimization routines failed to perform at a level we were satisfied with. Following this, we explored simulated annealing as an alternative optimization algorithm, which was used in our first paper [116, 63]. We have continued to refine the optimization algorithm to include informed guessing and develop a genetic optimization routine. These "informed guesses" include quadratic fits to one-dimensional marginals, for estimating μ and σ in each dimension.

While the final model is selected using the mean of the one- and two-dimensional KL divergences, we are able to make use of the individual KL divergences for each marginal. The initial population of the genetic algorithm is a set of informed guesses, filled with additional random guesses. At each time-step, *parents* are selected by considering the mean KL divergence. The *traits* passed down to the child population are the parameters of the multivariate normal fit, and are chosen randomly from the two parents *with a preference for the lower one- and two-dimensional KL divergences of associated marginals*. Following this, the child population is allowed to jump like a Metropolis-Hastings Markov Chain Monte Carlo (MCMC) random walker, which constitutes *mutation* [92]. At each step, the guesses with the lowest mean KL divergence are carried over to the breeding pool of the next generation.

Alongside our second paper, we provide a software package, GWALK (Gravitational-

| Parameterization | Coordinates | Prior |
|-------------------------|---|-------------------|
| aligned3d | $\mathcal{M}_{c,z}, \eta, \chi_{\text{eff}}$ | aligned3d |
| aligned3d_source | $\mathcal{M}_c, \eta, \chi_{\text{eff}}$ | aligned3d |
| aligned3d_dist | $\mathcal{M}_{c,z}, \eta, \chi_{\text{eff}}, l^{-1}$ | aligned3d_dist |
| mass_tides | $\mathcal{M}_{c,z}, \eta, \tilde{\Lambda}, \delta\tilde{\Lambda}$ | mass |
| mass_tides_source | $\mathcal{M}_c, \eta, \tilde{\Lambda}, \delta\tilde{\Lambda}$ | mass |
| aligned_tides | $\mathcal{M}_{c,z}, \eta, \chi_{\text{eff}}, \tilde{\Lambda}, \delta\tilde{\Lambda}$ | aligned3d |
| aligned_tides_source | $\mathcal{M}_c, \eta, \chi_{\text{eff}}, \tilde{\Lambda}, \delta\tilde{\Lambda}$ | aligned3d |
| aligned_tides_dist | $\mathcal{M}_{c,z}, \eta, \chi_{\text{eff}}, \tilde{\Lambda}, \delta\tilde{\Lambda}, l^{-1}$ | aligned3d_dist |
| spin6d | $\chi_{1x}, \chi_{2x}, \chi_{1y}, \chi_{2y}, \chi_{1z}, \chi_{2z}$ | precessing8d |
| precessing8d | $\mathcal{M}_{c,z}, \eta, \chi_{1x}, \chi_{2x}, \chi_{1y}, \chi_{2y}, \chi_{1z}, \chi_{2z}$ | precessing8d |
| precessing8d_source | $\mathcal{M}_c, \eta, \chi_{1x}, \chi_{2x}, \chi_{1y}, \chi_{2y}, \chi_{1z}, \chi_{2z}$ | precessing8d |
| precessing8d_dist | $\mathcal{M}_{c,z}, \eta, \chi_{1x}, \chi_{2x}, \chi_{1y}, \chi_{2y}, \chi_{1z}, \chi_{2z}, l^{-1}$ | precessing8d_dist |
| precessing_tides_source | $\mathcal{M}_c, \eta, \chi_{1x}, \chi_{2x}, \chi_{1y}, \chi_{2y}, \chi_{1z}, \chi_{2z}, \tilde{\Lambda}, \delta\tilde{\Lambda}$ | precessing8d |
| full_precessing_tides | $\mathcal{M}_{c,z}, \eta, \chi_{1x}, \chi_{2x}, \chi_{1y}, \chi_{2y}, \chi_{1z}, \chi_{2z}, \tilde{\Lambda}, \delta\tilde{\Lambda}, l^{-1}$ | precessing8d_dist |

Table 2.1: NAL parameterizations of the astrophysical properties associated with parameter estimation samples in the GWTCs.

Wave Approximate Likelihoods), at <https://gitlab.com/xevra/gwalk>. This package provides tools for constructing NAL for an arbitrary set of samples, within an arbitrary set of boundaries. It also provides a computationally efficient compiled Gaussian likelihood evaluation and our genetic optimization routine for NAL parameters.

2.3 Properties of NAL Models for GWTC Events

We find that NAL models for most events in the GWTCs are overwhelmingly in agreement with their associated sample density. These optimized models better represent the likelihood inferred from parameter estimation samples than Gaussians with assumed parameters based on the sample mean and covariance while providing the same efficient density evaluation and ease in generating randomly distributed samples. Additionally, the μ parameters of these models provide a more accurate MLE description of the astrophysical parameters for a given event than either the sample mean or median when significant boundary/truncation effects are in play. This is immediately relevant to astrophysical interpretations of gravitational-wave events, as boundary effects extend beyond a single parameter, and are unavoidable when fully characterizing the astrophysical parameters of a gravitational-wave event. The NAL model fits for the full parameterization of each waveform in the GWTC releases are available at <https://gitlab.com/xevra/nal-data>. The rest of this chapter considers the application and interpretation of these NAL models.

Most of the compact binaries reported in the GWTC releases are well constrained by source-frame chirp mass (\mathcal{M}_c), symmetric mass ratio (η), and aligned effective spin

(χ_{eff}) [6, 188, 51]. Other parameterizations are necessary to fully characterize events with properties different from the typical binary black hole merger, such as precessing spin and tidal deformability. Our choices for the parameterizations used for NAL models of a given event are given by table 2.1.

These parameterizations allow us to provide detailed and accurate models for the entire astrophysical parameter space for the gravitational-wave events reported in the GWTC releases for the third observing run of LIGO/Virgo, as well as a limited set of models for events in GWTC-1 which don't offer full spin information.

The labels representing the prior removed for each parameterization described in table 2.1 are all consistent with the prior choices described in section 2.1. However, the prior removed must represent the coordinates of a given parameterization, which differ from the aligned spin case to the precessing case, and for parameterizations that consider distance. The 'mass' prior removes only the prior in mass. The 'aligned3d' prior removes the prior in mass and χ_{eff} . The 'precessing8d' prior removes the prior in mass and Cartesian spin. The '_dist' suffix indicates that distance prior has been removed, as necessary for parameterizations which consider the inverse luminosity distance.

We have applied the NAL method to each set of samples available in the GWTC releases (GWTC-1: <https://dcc.ligo.org/LIG0-P1800370/public>, GWTC-2: <https://dcc.ligo.org/LIG0-P2000223/public/>, GWTC-2.1: <https://zenodo.org/record/5117762#.YwYrG9LMJB1>, GWTC-3: <https://zenodo.org/record/5546665#.YwYrHdLMJB1>) for each of the waveform models available for each set of samples (including IMRPhenomD [102, 112], IMRPhenomPv2 [91, 111], IMRPhenomPv3 [113], IMRPhenomPv3HM [149], IMRPhenomXPHM [163, 82, 162], SEOBNRv3 [154, 183], SEOBNRv4 [33], SEOBNRv4PHM [57, 150], and NRSur7dq4 [195], as well as others [138, 138, 65, 66, 95, 180]). These models support a wide variety of potential and realized applications.

2.3.1 Aligned Spin

As seen in figure 2.2, NAL models are in strong agreement with the GWTC samples. As the majority of events are near equal mass, the finite boundary effect of sample truncation in symmetric mass ratio ($\eta \leq 1/4$) introduces a significant bias away from equal mass in Gaussians assumed from the sample mean and covariance (fig 2.1). NAL models overcome this source of bias. For example, for the gravitational-wave event GW190521, we estimate $(\mu_{\text{opt}} - \mu_{\text{naive}})/\sigma_{\text{opt}} = 1.006$ for symmetric mass ratio, where μ_{opt} and σ_{opt} are parameters of the optimized NAL models and μ_{naive} is the sample mean. Some key events have been highlighted in figure 2.2 and table 2.2. As described in section 2.2.2, the mean value of the marginal KL divergences is used to characterize each fit.

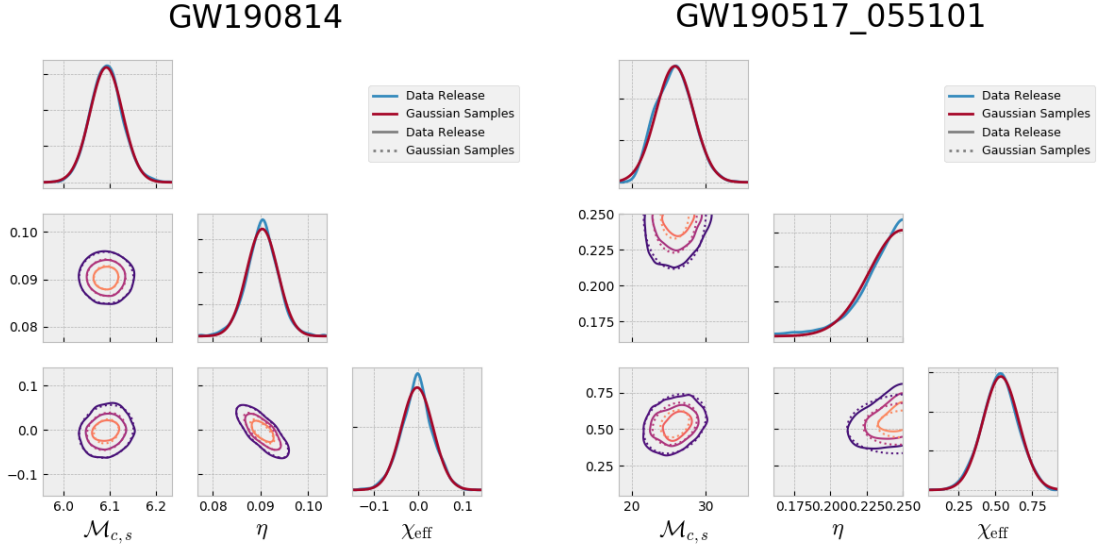


Figure 2.2: These corner plots are similar to figure 2.1, and represent optimized NAL fits for GW190814 and GW190517.055101 (again, through ‘PublicationSamples’). These are noteworthy events in GWTC-2, with GW190814 having a mass ratio significantly different from unity, and GW190517.055101 having a large spin magnitude.

| Event | KL | $\mu_{\mathcal{M}_c}$ | μ_{η} | $\mu_{\chi_{\text{eff}}}$ |
|-----------------|-------|---------------------------|---------------------------|---------------------------|
| GW150914 | 0.01 | $28.6^{+1.1}_{-1.1}$ | $2.500_{-0.007}$ | $0.00^{+0.09}_{-0.09}$ |
| GW170817 | 0.02 | $1.187^{+0.002}_{-0.002}$ | $0.247^{+0.003}_{-0.003}$ | $0.007^{+0.008}_{-0.008}$ |
| GW190403_051519 | 0.01 | $35.5^{+4.9}_{-4.9}$ | $0.17^{+0.03}_{-0.03}$ | $0.76^{+0.09}_{-0.09}$ |
| GW190425 | 0.02 | $1.43^{+0.01}_{-0.01}$ | $0.228^{+0.017}_{-0.017}$ | $0.09^{+0.05}_{-0.05}$ |
| GW190517_055101 | 0.005 | $25.8^{+2.5}_{-2.5}$ | $2.50_{-0.02}$ | $0.54^{+0.12}_{-0.12}$ |
| GW190521 | 0.016 | $65.6^{+6.5}_{-6.5}$ | $2.498^{+0.002}_{-0.022}$ | $0.06^{+0.23}_{-0.23}$ |
| GW190814 | 0.002 | $6.09^{+0.04}_{-0.04}$ | $0.090^{+0.003}_{-0.003}$ | $0.00^{+0.04}_{-0.04}$ |

Table 2.2: Optimized MLE properties of gravitational-wave events in the aligned-spin source-frame model. The goodness of fit is measured by the mean of the one- and two-dimensional KL divergences comparing each NAL model to each marginal (see section 2.2.2). The SEOBNRv3 approximant is used for GW150914, while the IMRPhenomPv2NRT_lowSpin approximant is used for GW170817, SEOBNRv4PHM is used for GW190403.051519, and ‘PublicationSamples’ is used for the remaining events.

| Event | KL | $\mu_{\mathcal{M}_c}$ | μ_{η} | $\mu_{\chi_{1z}}$ | $\mu_{\chi_{2z}}$ |
|-----------------|-------|-----------------------|----------------------------|------------------------|------------------------|
| GW190403_051519 | 0.009 | $36.0^{+5.4}_{-5.4}$ | $0.17^{+0.03}_{-0.03}$ | $0.91^{+0.09}_{-0.09}$ | $0.49^{+0.58}_{-0.58}$ |
| GW190517_055101 | 0.005 | $25.8^{+2.5}_{-2.5}$ | $0.2498^{+0.002}_{-0.003}$ | $0.66^{+0.19}_{-0.19}$ | $0.43^{+0.41}_{-0.41}$ |

Table 2.3: Single valued parameter estimates for gravitational wave events in the fully precessing Cartesian spin component source-frame model. Mean KL divergences are included to demonstrate the goodness of fit. SEOBNRv4PHM is used for GW190403.051519, and ‘Publication Samples’ is used for GW190517.055101.

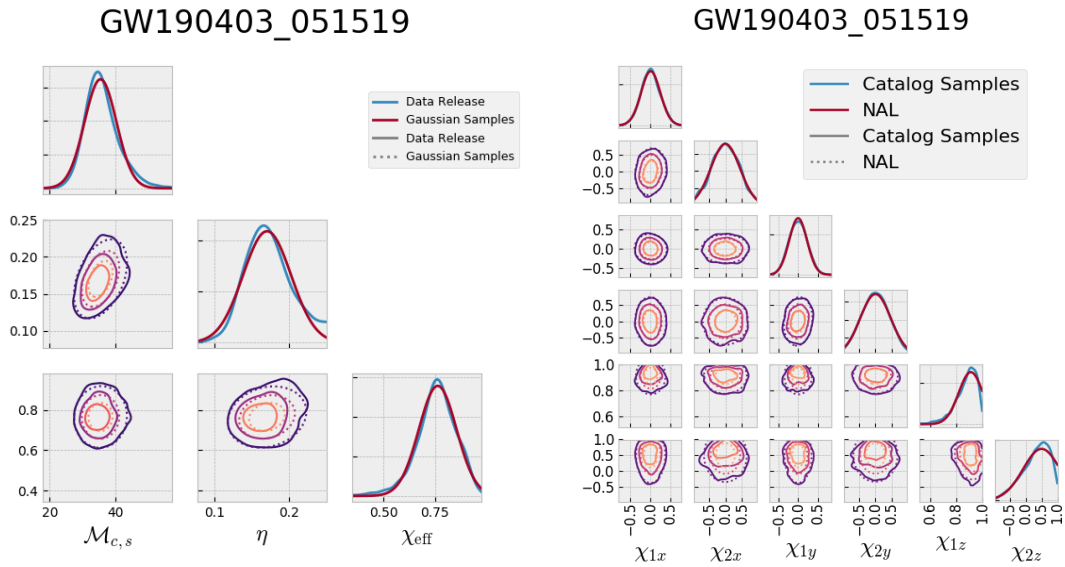


Figure 2.3: These corner plots are similar to figure 2.1, with (left) source-frame aligned spin parameters of GW190403_051519 and (right) Cartesian spin components for the same event. We study the SEOBNRv4PHM samples for this example. If this marginal detection is real, it has a nonzero spin by 10 characteristic standard deviations. We do note a minor disagreement in η (left) and with χ_{1z} and χ_{2z} (right), which we attribute to non-Gaussianity in our posterior samples.

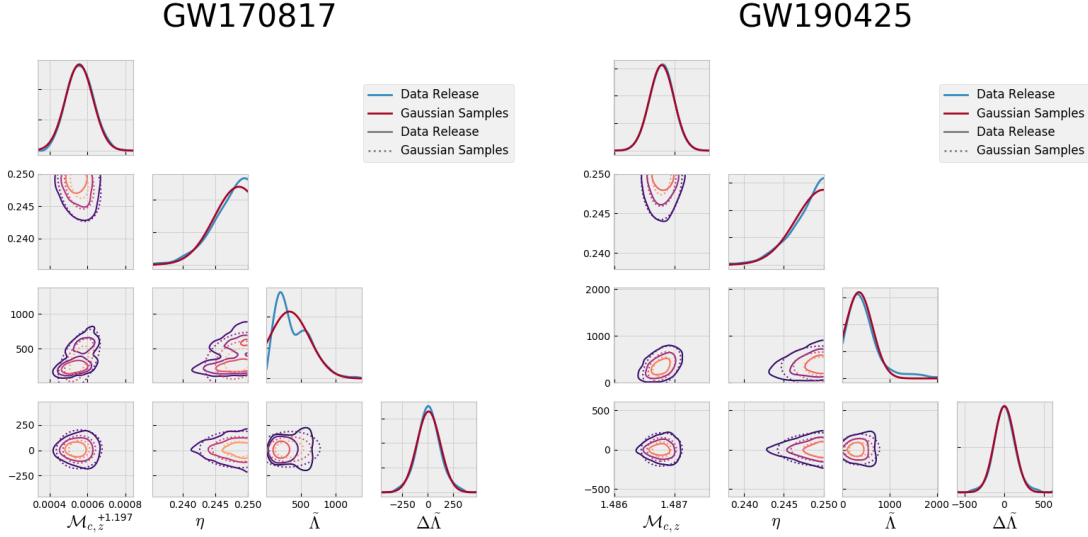


Figure 2.4: These corner plots are similar to figure 2.1, with tidal deformability parameterizations of BNS mergers (left) GW170817 and (right) GW190425. In this example in particular, we use detector-frame chirp mass to characterize each event. We consider the ‘IMRPhenomPv2NRT_lowSpin’ samples for GW170817 and the ‘AlignedSpinInspiralTidal_LS’ samples for GW190425. We note significant non-Gaussianity in the sample distribution for GW170817, which explains the limitations of the NAL model in fully characterizing these sample distributions.

2.3.2 Precessing spin models

NAL models are in strong agreement with the GWTC samples, providing well-posed likelihood models for aligned and precessing spin. As seen in figure 2.3, NAL models overcome the finite boundary (truncation) effect of spin magnitudes ($\chi < 1$ for physical systems) for events with high spin. While few events are known to have high spin, there are well-constrained examples of such events, and of events with precessing spin components [185, 9]. As a system with a spin magnitude $|\chi| \geq 1$ is not physical (representing a naked singularity in the case of a black hole), we must consider this another finite boundary limitation of our model. NAL optimization overcomes this boundary effect as well, with $(\mu_{\text{opt}} - \mu_{\text{naive}})/\sigma_{\text{opt}} = 0.43$ for GW190403_051519 and 0.28 for GW200115_042309 for χ_{1z} , for example. We provide NAL models for the full six-dimensional Cartesian spin component model for each event where parameter estimation samples in the GWTC releases support such a decomposition.

2.3.3 Tidal Parameters

As seen in figure (2.4), NAL models support tidal deformability parameterizations as well, and these are also in strong agreement with the GWTC samples. We provide NAL

| Event | KL | $\mu_{\mathcal{M}_c}$ | μ_η | $\mu_{\tilde{\Lambda}}$ | $\mu_{\delta\tilde{\Lambda}}$ |
|----------|------|---------------------------------|---------------------------|-------------------------|-------------------------------|
| GW170817 | 0.02 | $1.19756^{+0.00007}_{-0.00007}$ | $0.249^{+0.001}_{-0.004}$ | 332^{+291}_{-291} | $9.484^{+0.011}_{-0.011}$ |
| GW190425 | 0.02 | $1.4874^{+0.0004}_{-0.0004}$ | $0.23^{+0.02}_{-0.02}$ | 208^{+884}_{-208} | 37^{+192}_{-192} |

Table 2.4: Single valued parameter estimates for gravitational wave events in the mass-tides parameterization. Mean KL divergences are included to demonstrate the goodness of fit. The SEOBNRv3 approximant is used for GW150914, while the IMR-PhenomPv2NRT_lowSpin approximant is used for GW170817.

models with tidal parameterizations indiscriminately for event/waveform combinations in the GWTC releases which offer support for tidal information, including the two BNS mergers, GW170817 and GW190425 [5, 7]. We adopt the standard parameterization of $\tilde{\Lambda}$ and $\delta\tilde{\Lambda}$ from Wade et al. [199]:

$$\tilde{\Lambda} = \frac{8}{13} \left[(1 + 7\eta - 31\eta^2)(\Lambda_1 + \Lambda_2) + \sqrt{1 - 4\eta}(1 + 9\eta - 11\eta^2)(\Lambda_1 - \Lambda_2) \right] \quad (2.7)$$

$$\delta\tilde{\Lambda} = \frac{1}{2} \left[\sqrt{1 - 4\eta} \left(1 - \frac{13272}{1319}\eta + \frac{8944}{1319}\eta^2 \right) (\Lambda_1 + \Lambda_2) + \left(1 - \frac{15910}{1319}\eta + \frac{32850}{1319}\eta^2 + \frac{3380}{1319}\eta^3 \right) (\Lambda_1 - \Lambda_2) \right] \quad (2.8)$$

For clarity, figure 2.4 showcases only the mass parameters of these fits, in detector-frame coordinates. NAL models overcome the finite boundary effect introduced by truncation for $\tilde{\Lambda} > 0$. For GW190425, for example, the boundary effect removed can be estimated by $(\mu_{\text{opt}} - \mu_{\text{naive}})/\sigma_{\text{opt}} = 0.72$. We include an example, demonstrating that NAL models apply to high-dimensional parameterizations of the astrophysical properties of gravitational-wave events in figure 2.5, exploring detector-frame mass parameters, Cartesian spin, tidal deformability, and inverse luminosity distance.

2.4 Applications of NAL Models

NAL models provide a compact likelihood approximation for the astrophysical properties of each gravitational-wave event published in the GWTC releases. They further provide insight into those astrophysical properties for individual events through MLE characterizations of the parameters representing those properties. They also overcome bias introduced when assuming a Gaussian from the sample mean and covariance. Together, these models further provide an understanding of the population of gravitational-wave events released so far, and our methods have broader applications such as population inference (as we will see in the next few chapters) and parameter estimation.

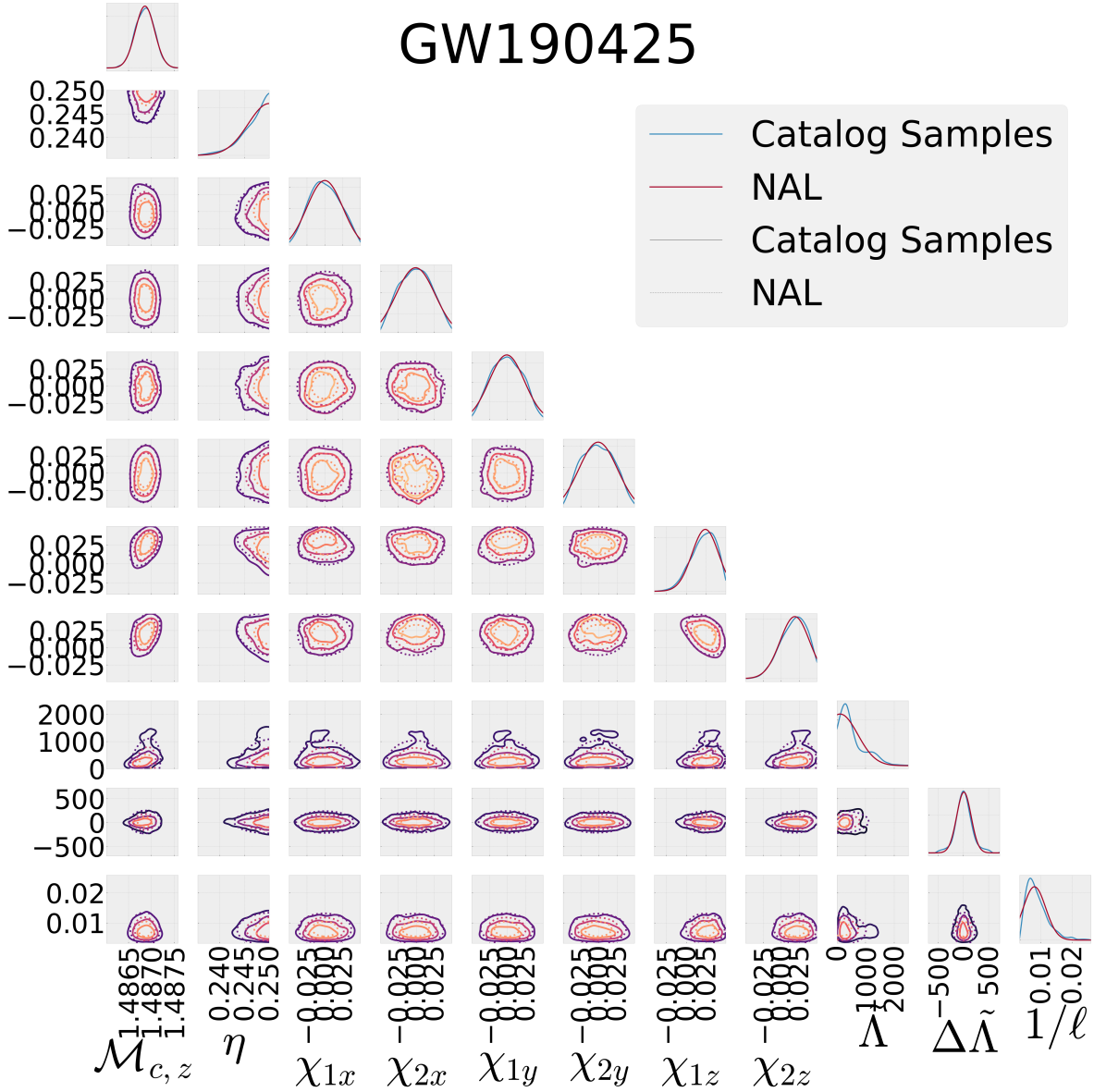


Figure 2.5: This corner plot is similar to figure 2.1, including the full eleven-dimensional parameterization for the detector-frame masses, Cartesian spin components, tidal deformability, and inverse luminosity distance. For this example, ‘IMRPhenomPv2_NRTidal-LS’ samples are used. Despite some minor non-Gaussianities, the NAL model fits the samples well.

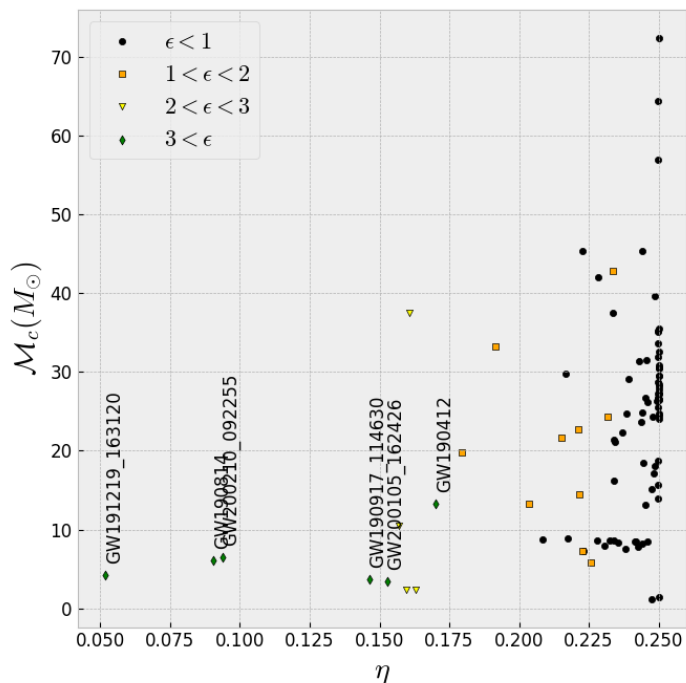


Figure 2.6: MLE aligned-spin source-frame estimates in \mathcal{M}_c and η for all marginal and confident detections in the GWTC releases. Markers indicate deviation from equal mass ($\epsilon = (1/4 - \mu_{\text{opt}})/\sigma_{\text{opt}}$).

2.4.1 Properties of the Gravitational-Wave Population

Through GWTC-3, the gravitational-wave population is reported to be biased toward equal mass [51]. However, the sample-mean estimates tabulated for the properties of each event in the GWTC papers don't provide an effective MLE representation of the symmetric mass ratio, which waveform models are especially sensitive to. Figure 2.6 demonstrates the NAL maximum likelihood estimates of each event (marginal and confident), in source-frame chirp mass and symmetric mass ratio. Our parameterizations of each likelihood model allow us to estimate how many σ each event is in difference from equal mass. This quantity is related to the half-width-half-max of our distribution, and is a characteristic estimate of the standard deviation expected of the Gaussian without a boundary (used to classify the error of measurements as σ , 2σ , 3σ etc...).

In addition to MLE characterizations, we can also describe the population using the truncated Gaussians in various ways. For example, figure 2.7 arranges the Cumulative Distribution Function (CDF) for the gravitational-wave population through GWTC-3, using only the confident detections (consistent with [51]). For this arrangement, the one-dimensional marginal for the source-frame chirp mass is used for a variety of approximants.

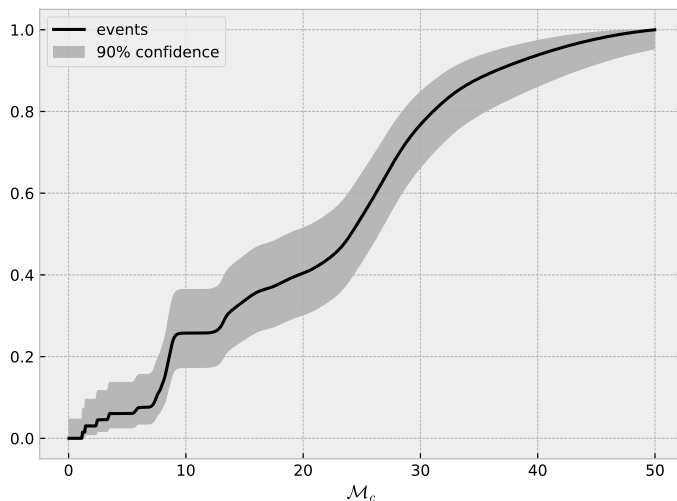


Figure 2.7: The CDF for the gravitational-wave population, estimated using NAL models with a Wilson Score interval [202], including only those events in the LSC’s O3b population paper [51].

2.4.2 Applications for Low-Latency Parameter Estimation

Our method can ultimately be applied not only to the secondary parameterization of released samples, but also directly to parameter estimation routines. The NAL optimization can be carried out using either a set of draws from the posterior of a given event (as done throughout this chapter) or a set of likelihood evaluations. Even a sparse set of evaluations can be used to efficiently generate NAL models, making NAL a candidate for the rapid characterization of binary sources in-situ during an observing run.

Figure 2.8 provides a simplistic example of this potential low-latency application. The RIFT inputs provide a limited set of likelihood evaluations through IMRPhenomD, using marginalized detector-frame mass and spin distributions. This evaluation set is chosen in the range of binary parameters flagged during an observing run, for low-latency followup for a potential electromagnetic counterpart. As most potential electromagnetic follow-ups in the near future are expected to occur at low redshift, a detector-frame mass parameterization is employed in this example. The optimization routine for this example is simplified so as to not select parameters for the *child* population using information about the one- and two-dimensional marginals, as these are not computed for a grid of likelihood evaluations. The NAL optimization in this example is carried out in a few seconds, including the overhead costs of initializing the program.

The exceptional, uninformed, agreement of the low-latency NAL optimization (figure 2.8) with the published GWTC samples demonstrates the possibilities our method holds for low-latency parameter estimation application. However, further work must be done for a systematic justification of this method for potential low-latency parameter

GW190412

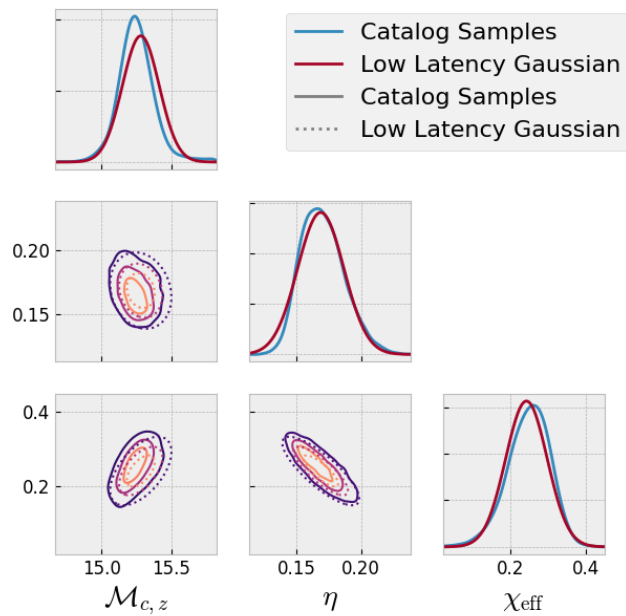


Figure 2.8: A NAL (detector-frame) characterization of GW190412, using a sparse set of likelihood evaluations from RIFT (with IMRPhenomD), designed to imitate the availability of evaluations in a low-latency setting. The GWTC sample estimate provided for comparison are the “PublicationSamples” provided in the GWTC-2 release.

estimation.

Chapter 3

Simulating the Evolution of Massive Binary Star Systems

In this chapter, I provide a brief overview of the binary evolution of massive stars, focusing on the processes which are characterized in this dissertation and related work. I will begin with a brief review of the literature for massive stellar binaries. Following this, I will describe our use of the StarTrack algorithm used to produce the population of simulated mergers associated with the formation channel for compact binaries. I will demonstrate the processing required to construct a physically justified population of merging binaries to be consistent with those observed by gravitational-wave observatories. Finally, this chapter will also include a discussion of the StarTrack synthetic universe data products, as well as their physical significance.

3.1 The Evolution of Massive Stars and Binaries

We summarize the well-studied life cycle of massive stars; see Hurley et al. (2000) for a review [99]. See also other related works [47, 115, 206]. When a star is born, it will reach a thermodynamic equilibrium with the nuclear reactions that power it; i.e. the fusion of hydrogen into helium. Once this equilibrium is achieved, we say that a star has reached the Zero Age Main Sequence (ZAMS), where its mass, metallicity, and rotation become sufficient to determine a star's isolated evolution. This is the starting point for the study of stellar evolution.

A star spends most of its life on the main sequence, fusing hydrogen in its core. Following this, the course of a star's evolution depends largely on its mass. The least massive stars ($0.08M_{\odot} < m < 0.8M_{\odot}$) never fully expend the hydrogen at their cores, and continue to burn hydrogen slowly, conserving their fuel for potentially trillions of years. Stars in the ($0.8M_{\odot} < m < 8M_{\odot}$) will have a shorter lifetime, entering the red

giant and asymptotic giant branch stages before ending their lives as white dwarfs with planetary nebula.

A massive star ($M > 8M_{\odot}$) will leave the main sequence even sooner, as a supergiant. As giant and supergiant stars cool and expand, they lose a substantial amount of mass to stellar wind. They may also shed the outer layers of its atmosphere entirely, becoming an exposed helium core or Wolf-Rayet star. Further nuclear reactions are endothermic, and the star's core will collapse as electron degeneracy pressure is lost. The end of such star's life is a type II supernova explosion, the result of which is a compact remnant (a neutron star or a black hole).

It is expected that about two thirds of massive stars belong to a binary system [26]. These binary systems are bound together by the gravitational binding energy of their orbit and separated by the orbital angular momentum. For those systems of massive stellar binaries in tightly bound orbits, several of effects can determine if they remain separated for their lifetime, or if enter a phase of mass transfer (accretion), enter a phase where they share a common envelope of external atmosphere, or merge as luminous companions or compact remnants with a detectable gravitational radiation signature. The rest of section 3.1 will explore how these processes are modeled, in order to predict how stars and stellar binaries evolve.

Stellar Wind

Stellar wind is material ejected from a stellar atmosphere as gas and dust without substantial clumping. Stellar wind is key to the volumetric mass loss rate of stars. Understanding it requires a study of stellar atmosphere models. Various groups have studied mass loss due to stellar wind in the evolution of massive stars [32, 141, 90, 197, 148, 41, 133, 165]. In addition to its role in stellar evolution, some stellar wind can be captured by a binary companion, effecting binary evolution [32, 27, 24].

The initial mass and metallicity of a star are expected to play a major role in the amount of matter ejected by stellar wind, with substantially weaker stellar winds present in main sequence stars at low metallicity [148, 165, 24]. This is known as the “weak-wind phenomenon,” which is an ongoing area of research, and may determine if a star enters a Wolf-Rayet phase or not [165]. However, this phenomenon does not substantially impact volumetric mass loss rates during the supergiant phase of massive stars [165].

3.1.1 Supernova Engines

The death of a massive star through a core-collapse supernova has been studied in-depth by many groups [77, 144, 127], and we attempt to briefly characterize the supernova mechanisms. It is important to understand these processes when studying the formation channels for compact binaries, as different models are capable of producing black holes and neutron stars in different mass ranges, and with different properties. It was common knowledge that black holes should not form in the lower mass gap ($2.5 - 5 M_{\odot}$), in a

vacuum, until gravitational-wave events were observed with masses in that range (e.g. GW190814; although it was proposed that black holes could form in that range due to interactions with a binary companion of similar ZAMS mass) [187].

As the runaway nuclear reactions in massive stars become endothermic, the core of a massive star begins to collapse. This collapse is halted by nuclear forces, as a proto-neutron star core forms with the density of an atomic nucleus. Infalling material during this collapse can have velocities near the speed of light, and the formation of the proto-neutron star core halts this infalling material, producing shocks that reverberate throughout the convective envelope of the star. The proto-neutron star continues to leak energy through neutrino emission, as neutrinos are particles which carry mass and can escape from dense regions where light is blocked by the stellar atmosphere. The shocks carry energy away from the core until they are damped by neutrino emission. Instabilities in the region where these shocks propagate can result in energy instead being transformed into kinetic energy, pushing the envelope away from the core. This kinetic energy is the cause of the energetic ejection of material associated with the supernova. The time taken by the ejection of the convective envelope determines the amount of matter which can accrete onto the proto-neutron star core, and ultimately determines the fate of the compact remnant.

Groups such as Fryer et al. have proposed rapid and delayed convection-enhanced neutrino-driven supernova explosion models [77]. The “rapid” supernova engine predicts a lower mass gap for black holes, as stars undergoing a core-collapse supernova with a “rapid” convective timescale are unable to produce compact remnants in the $2.5 - 5M_{\odot}$ range. The “delayed” supernova engine does not exhibit the same properties and is capable of producing black holes in this region [77, 28].

There are other types of supernovae which can occur for the most massive stars ($M > 80M_{\odot}$) [127]. For these stars, energetic gamma rays are produced during the formation of the oxygen core, the absorption of which causes electron-positron pair production. This causes a contraction of the core, resulting in an accelerated oxygen burning phase. For stars with more than $150M_{\odot}$, this accelerated oxygen burning becomes a runaway thermonuclear explosion, annihilating the star in a Pair-Instability SuperNovae (PISN), leaving no compact remnant. For stars in the $80M_{\odot} < M < 150M_{\odot}$ range, the energy released by pair-instability is insufficient to trigger a PISN. These stars release energetic pulses during the pair-instability phase, shedding mass until they no longer produce the energetic gamma rays required for pair-instability, and ultimately undergo core-collapse supernovae. Systems which undergo this Pulsational Pair Instability (PPI) before core-collapse are labeled as PPI SuperNovae (PPISNe).

The effect of PISN and PPISN on the population of compact remnants is the prediction of an upper limit on low-mass black holes, around $50M_{\odot}$, known as the “upper mass gap.” The mass ranges for which PISN and PPISN can occur depend on the rotation and the ZAMS metallicity of massive stars, as well as models of mass loss due to stellar wind [127].

Supernova Recoil Kicks

Asymmetries in ejected material during a supernova can impart linear momentum on a compact remnant, which results in a “recoil kick” for the compact remnant, with some velocity. The strongest evidence for supernova recoil kicks is that the velocity distribution of neutron stars is much greater than that of the stellar populations which produce them [88, 44, 144]. Observationally, there is further support for recoil kicks in both gravitational-wave measurements [151] and electromagnetic sources [87, 161]. For neutron stars, this effect is equal to the linear momentum of the ejected material [53, 96]. Belczynski et al. (2002) found that a second Maxwellian component is a good predictor for pulsars with high kick velocities [26]. For black holes, the imparted linear momentum is reduced by the fraction of the ejected material that falls back onto the black hole [54, 77]. Recently, different groups have found support for substantial asymmetries in supernova engines driven by neutrinos, using independent simulation and analysis [205, 77, 143].

3.1.2 Interacting Binaries and the Common Envelope Phase

Different mechanisms are expected to enable mass transfer between binary companions as well as mass ejection from binary systems, including the Common Envelope (CE) phase as well as stellar wind, clumped ejection, and other means. These interactions typically involve the transfer of mass from one star (the donor) to its companion (the accretor). The most significant of these interactions is the ejection of a common envelope by means of non-conservative mass transfer, which is essential to our understanding of how compact objects form [34, 153, 167, 168, 129, 157, 26].

Common envelope evolution can result in compact binaries, cataclysmic variable stars, Type Ib supernova, naked helium stars, or a complete merger without the formation of a compact binary [153, 118]. In particular, the formation channel for compact binaries which may merge to produce gravitational radiation involves a rapid inspiral of the companion object inside the shared envelope, which leads to the ejection of the common envelope. There are not many other known mechanisms by which compact binaries may experience the necessary orbital shrinkage to merge by emission of gravitational radiation within the age of the known Universe. Conversely, if the common envelope remains bound, the binary components merge completely without forming a compact binary.

A successful CE ejection occurs when the remnant core of the giant donor star is smaller than its Roche-lobe, and depends largely on the original mass, radius, and metallicity of the donor star, as well as a choice of common envelope efficiency α_{CE} , and an envelope structure constant λ_{CE} [209, 38, 78, 135, 160, 184, 159, 89, 104, 103, 200, 118, 27, 30, 39, 203]. The energy stored in a common envelope can be calculated by considering the gravitational potential energy of the envelope together with thermal and chemical energies. By modeling the gravitational potential energy of the common envelope and core of the donor star separately, we can calculate the post-CE separation

of a binary while freely varying both λ_{CE} and α_{CE} [118].

Mass transfer instability plays a crucial role in this process, affecting the structure of the common envelope as well as the distance between the core of each companion. Mass transfer becomes unstable when the donor star’s Roche-lobe shrinks faster than the size of the donor, and is the result of a non-conservative method of mass transfer on behalf of the donor [157]. This type of non-conservative mass transfer necessarily occurs only in systems with a mass ratio satisfying $q_{crit} < q < 1.0$, for some q_{crit} [157]. Rather than a pre-determined constant of our evolution model, q_{crit} is constrained by the population of merging binaries. If mass transfer occurs after the hydrogen core burning phase, but before the ignition of central helium, and the primary fills its Roche lobe, then $q_{crit} \approx 0.97$ [12, 192]. Alternatively, if mass transfer occurs after the initial primary’s helium burning phase, $q_{crit} \approx 0.9$. Supernova recoil kick velocities have a large impact on the outcome of such mass transfer associated with a common envelope ejection, as radially symmetric supernovae are more likely to cause a binary system to become unbound [20].

Here, we describe the formalism for this type of non-conservative mass transfer, as seen in Rappaport, Joss, and Webbink (1982), and Rappaport, Verbunt, and Joss (1983) [167, 168]. This process is specified by two free parameters: The fraction f_a , of the mass lost by the doner, that is accreted by star 2, and the specific angular momentum β , of any matter lost from the system, in units of $2\pi a^2/P$.

$$\delta J = \beta \delta \dot{M}_1 (1 - f_a) \frac{2\pi a^2}{P} \quad (3.1)$$

where $\delta \dot{M}_1$ is infinitesimal mass lost by the initial primary, and δJ is a small amount of angular momentum held by matter ejected by the system, a is the semimajor axis, and P is the orbital period [157]. Values of f_a less than unity indicate mass is lost from the system (due to ejected material). Podsiadlowski et al (1992) [157] argue that if the common envelope is in thermal equilibrium, the final properties of the binaries depend only on the final masses of the hydrogen-exhausted core and hydrogen-rich envelope.

3.2 Simulating Populations of Massive Binaries with StarTrack

Many groups have developed binary evolution simulations to produce synthetic populations of compact binaries, including the COMPAS software [181, 169, 39, 40] and POSYDON [75]. The POSYDON group (Fragos et al) [75] have organized a list including many of these other software [105, 106, 107, 72, 193, 194, 100, 124, 36, 85, 128, 179, 191, 190]. Throughout the rest of this dissertation, the work summarized includes the StarTrack binary evolution simulations [26, 27, 25, 28].

The StarTrack algorithm reproduces a physically motivated population of massive stellar binaries for a population with a specified metallicity and initial mass function. The merger rate densities represented by these populations can be used to generate synthetic universes which predict the compact binaries formed in the history of The Universe, accounting for changes in the metallicity of The Universe over cosmological time [68]. StarTrack accounts for many physical processes, including stellar evolution, accretion, tidal interactions, stellar wind, metallicity, gravitational radiation, magnetic braking, and recoil kicks. The content in this section is based on prior work [26, 27, 25, 28, 67, 68, 69, 208].

Each run of StarTrack begins with a set of assumptions about the physical processes involved in the formation and evolution of binary star systems which could produce compact binaries. In many cases, these assumptions are characterized by a formation parameter assumed inductively. The set of these formation parameters defines the independent variable space of our simulations, which we call Λ .

3.2.1 Initial Mass Function

A StarTrack synthetic universe is generated as a set of distinct runs of the core StarTrack algorithm, each corresponding to a cosmological reference time. Each such run is generated as a fixed number of isolated binaries at a fixed reference time. The primary component of each binary is drawn from a Kroupa Initial Mass Function (IMF) [172, 122, 123].

$$\Psi(M_1) \propto \begin{cases} M_1^{-1.3} & 0.08M_\odot \leq M_1 < 0.5M_\odot \\ M_1^{-2.2} & 0.5M_\odot \leq M_1 < 1.0M_\odot \\ M_1^{-\alpha_{IMF}} & 1.0M_\odot \leq M_1 < 150M_\odot \end{cases} \quad (3.2)$$

where we adopt $\alpha_{IMF} = 2.35$, consistent with the literature [28, 117]. The companion mass is drawn from a uniform distribution in mass ratio, for $q_{\min} \leq q \leq 1$. [119, 22, 70]. A value of $q_{\min} = 0.08M_\odot/m_1$ represents the smallest allowed companion corresponding to the hydrogen-burning limit [119]. Following Belczynski et al. (2020) [28], we adopt a value for $q_{\min} = 0.1M_\odot/m_1$. Only systems for which $m_1 > 5M_\odot$ and $m_2 > 3M_\odot$ are evolved in a StarTrack run, as only these systems are expected to form compact binaries.

This population of stars is representative of some amount of star-forming gas, M_{sim} , which must account for systems in the mass cutoff region, systems which do not form binaries, and systems which do not merge in the age of The Universe. The contribution for systems outside the mass cutoff for potential compact binaries must be described by a mass efficiency, λ_{eff} , [152].

$$\lambda_{\text{eff}} = \frac{n}{N} \frac{f_{\text{cut}}}{\langle M \rangle} \quad (3.3)$$

where N binaries are simulated out of n progenitor systems, $\langle M \rangle$ is the average mass of all binary progenitors, and where f_{cut} accounts for the proportion of the IMF in the cutoff region.

The true fraction of stars, f_{bin} , which belong to binary systems is not known. We compare the merger rate per unit mass at a given time, marginalized over merger parameters, $\rho_{\Lambda}(t|f_{\text{bin}})$, to a reference value where $f_{\text{bin}} = 1$. This way, we can rescale the merger rate for an arbitrary choice of f_{bin} [152]:

$$\rho_{\Lambda}(t|f_{\text{bin}}) = \rho_{\Lambda}(t|f_{\text{bin}} = 1) \frac{f_{\text{bin}}(1 + \langle q \rangle)}{1 + f_{\text{bin}}\langle q \rangle} \quad (3.4)$$

For our purposes, $\langle q \rangle$ is assumed to be one, and f_{bin} is assumed 1/2.

Finally, we can compute M_{sim} , the mass represented by the represented population of StarTrack binaries:

$$M_{\text{sim}} = \frac{2f_{\text{bin}}}{1 + f_{\text{bin}}} \frac{n}{N} \frac{f_{\text{cut}}}{\langle M \rangle} M_{\text{bin}} \quad (3.5)$$

This mass estimate allows us to rescale the population of binary systems evolved by the StarTrack algorithm to match the size of a galaxy, or the physical universe. Each metallicity bin evolves $N = 2 \times 10^6$ binary systems [28].

3.2.2 Single Star Evolution Assumptions

StarTrack relies extensively on the work of Hurley, Pols, & Tout (2000), for the evolution of massive stars, summarized in section 3.1 [99]. Individual stars evolve following from Hurley, Pols, & Tout (2000) [99], whereby an individual star’s zero-age main sequence mass and metallicity are sufficient to predict its evolution. Consistent with Belczynski et al. (2020) [28], we explore a variety of supernova engine settings, based on the work of Fryer et al. (2012) [77] and Leung, Nomoto, and Blinnikov (2019) [127], including rapid and delayed models which account for pair-instability. We explore a parameter space in σ_{kick} , the characteristic recoil kick velocity for a single Maxwellian distribution representative of asymmetric neutrino-driven supernova ejecta.

Stellar Wind

The StarTrack algorithm models stellar wind as an accretion process, following Bondi & Hoyle (1944) and Boffin & Jorissen (1988) [34, 32, 27]. To address the weak-wind phenomenon, StarTrack makes use of global scale factors of $f_{\text{wind1}} \leq 1.0$, and $f_{\text{wind2}} \leq 1.0$, which multiplies the assumed volumetric mass loss rate due to stellar wind [24]. Here, f_{wind1} applies to hydrogen-dominated stars, while f_{wind2} applies to helium-dominated stars (such as naked helium cores). In our work, we vary these factors together ($f_{\text{wind1}} = f_{\text{wind2}}$), but this is not a necessary assumption.

3.2.3 Binary Evolution

The StarTrack binary evolution algorithm considers not only individual stellar evolution, but also an up-to-date model of the effects of stellar evolution on binaries, consistent with literature (see section 3.1) [28]. StarTrack makes standard assumptions about the initial separation of binary systems [11]. As we are interested in only systems which can become merging compact binaries, the evolution of systems where the donor mass falls below $0.5M_{\odot}$, or when the companion falls below $0.3M_{\odot}$ during mass transfer is discontinued.

Formation Parameters

In our own work, we use StarTrack simulations like those described in Belczynski et al (2020) [28]. The models we study are variations with particular choices for some of the formation parameters assumed as inputs for the StarTrack simulations. For instance, we vary our assumptions in the accretion fraction f_a and specific angular momentum β associated with non-conservative mass transfer during common envelope evolution (see 3.1).

Consistent with Belczynski et al (2020) [28], the binding energy parameters α_{CE} and λ_{CE} are set constants where $\alpha_{CE} = 1$ and $\lambda_{CE} = 0.1$. The value α_{CE} is consistent with prior literature, and is supported by modern work [38, 78, 135, 160, 184, 159, 89, 28, 203]. The value of the structure constant is expected to be consistent with more massive stars, such as those which can form compact binaries [209, 200, 28].

Spinning Binaries

Previous work has indicated that the final spin of compact binary mergers originating from isolated binary evolution does not depend on initial stellar rotation or metallicity [80, 131, 79, 28]. The final spin of such a compact binary is thought to depend more on the process by which angular momentum is transported within the system. Belczynski et al. have done recent studies on spin distributions in the population of compact binaries generated by the StarTrack binary evolution simulations [28]. In this work, we do not consider these spin models.

3.3 Cosmological Postprocessing

As stated previously, a synthetic universe is not one run of StarTrack, but several, at different metallicities [68, 28]. Each run of StarTrack is at a fixed metallicity, and simulates an epoch of steady star formation, Δt in cosmological time. We now summarize the work of Belczynski et al. [28], to describe the synthesis of a synthetic universe using multiple StarTrack runs at different assumed metallicities.

3.3.1 Estimating a Merger Rate

Each run of StarTrack outputs a set of sample mergers, occupying a compact binary merger parameter space, λ , which will have some associated density $\rho_{\Lambda, \mathcal{Z}}(\lambda)$, where Λ is the set of physical assumptions about the formation parameters of merging compact binaries, and \mathcal{Z} is the assumed metallicity. When desired, this density is normalized over the population to describe a dimensionless probability distribution, characterized by $N_{\Lambda, \mathcal{Z}}$: the integrated value of the physically motivated density over the entire sample.

$$N_{\Lambda, \mathcal{Z}} = \int_{\lambda} \rho_{\Lambda, \mathcal{Z}}(\lambda) d\lambda \quad (3.6)$$

We now follow along the outlined procedures described in section 2.6 of Belczynski et al. (2020) [28]. Therefore, we adopt the Madau & Fragos (2017) star formation rate variability on redshift (z), with an IMF-dependent correction factor [132]:

$$\text{SFR}(z) = \mathcal{K}_{\text{IMF}} 0.0015 \frac{(1.0 + z)^{2.7}}{1.0 + ((1.0 + z)/3.0)^{5.35}} \text{M}_{\odot} \text{Mpc}^{-3} \text{yr}^{-1} \quad (3.7)$$

Here, $\mathcal{K}_{\text{IMF}} = 0.66$ is a correction factor, which readjusts the star formation rate to match the Salpeter IMF. We also adopt the Madau & Fragos mass-metallicity relationship, satisfying $\log(\mathcal{Z}/\mathcal{Z}_{\odot}) = 0.153 - 0.074z^{1.34}$, where $\mathcal{Z}_{\odot} = 0.017$.

Each chunk Δt is characterized by a sample of galaxies from a Schechter-type probability density function, frozen at redshift $z = 4$, including 10^4 such galaxies [174, 73, 68]. Each galaxy is assigned a metallicity, according to a relationship assumed for the dependency of metallicity on redshift (see [132]), with 0.5 dex simulated Gaussian noise. These galaxies are gathered into metallicity bins, and the mass of each bin is calculated, $M_{\Lambda, \mathcal{Z}, \Delta t}$. The metallicity bins used in our studies are $\mathcal{Z} \in \{0.0001, 0.0002, 0.0003, 0.0004, 0.0005, 0.0006, 0.0007, 0.0008, 0.0009, 0.001, 0.0015, 0.002, 0.0025, 0.003, 0.0035, 0.004, 0.0045, 0.005, 0.0055, 0.006, 0.0065, 0.007, 0.0075, 0.008, 0.0085, 0.009, 0.0095, 0.01, 0.015, 0.02, 0.025, 0.03\}$ [28].

Each metallicity bin requires a separate StarTrack simulation, but these metallicity bins are consistently organized across different time steps Δt . In principle, it may be useful at this step to create a merger density $\rho_{\Lambda}(\lambda, t, \mathcal{Z})$, by isolating $\rho_{\Lambda, \mathcal{Z}}(\lambda)$ at each time step. To conserve computation, we refrain from doing this. Instead, we construct a weight function for the merger rate in a particular time step, for each metallicity bin:

$$\rho_{\Lambda, \mathcal{Z}, \Delta t}(\lambda) = \frac{M_{\Lambda, \mathcal{Z}, \Delta t}}{M_{\Lambda, \{\mathcal{Z}\} \Delta t}} \frac{\text{SFR}(z)}{M_{\text{sim}}} \quad (3.8)$$

Following this, a discrete marginalization yields the merger density for a synthetic

universe:

$$\rho_{\Lambda}(\lambda) = \sum_{\Delta t, \mathcal{Z}} \rho_{\Lambda, \mathcal{Z}, \Delta t}(\lambda) \Delta t \Delta \mathcal{Z} \quad (3.9)$$

This density function is scaled physically to represent merging binaries in 1 cubic megaparsec (Mpc^3) in one year, with a correctly justified distribution in metallicity, and scaling in mass. Hence, ρ_{Λ} has units of mergers $\text{Mpc}^{-3}\text{yr}^{-1}$.

3.3.2 Predicting the Gravitational-Wave Detection Rates

While the merger rate, $\rho_{\Lambda}(\lambda)$ is useful in its own rite, we are primarily interested in those simulated mergers which could be detected by current instrumentation. We use a simplified detection model, considering observable simulated detections to require a Signal to Noise Ratio (SNR) of at least eight, using an interpolated SNR consistent with the LSC's predictions for instrument sensitivity (see [186]) for a single detector network. We define a detection rate, $R(\lambda)$ for a sample merger, as

$$R_{\Lambda}(\lambda) = \rho(\lambda) p_{\text{det}}(\lambda) \frac{dV_c}{dz_m} \frac{dt_m}{dt_{\text{det}}} \quad (3.10)$$

where $dt_m/dt_{\text{det}} = 1/(1+z_m)$ is the factor relating merger time and detection time. p_{det} is related to the LIGO sensitivity, and is interpolated from a table tabulated by other groups [69]. Finally, we also use

$$\frac{dV_c}{dz_m} = \frac{4\pi c}{H_0} \frac{D_c^2(z)}{E(z)} \quad (3.11)$$

where $D(z)$ is the comoving distance and $E(z)$ is a cosmological scale factor [69].

The expected number of gravitational-wave detections for a given type of observation (BBH, BNS, NSBH) is calculated using that density according to Dominik et al. [69]:

$$\mu_{\Lambda, \alpha} = T_{\text{obs}} \mathcal{R}_{\Lambda, \alpha} = \int_0^{\infty} \int \int R_{\Lambda, \alpha}(m_1, m_2, z_m) dz_m dm_1 dm_2 \quad (3.12)$$

where $R_{\Lambda, \alpha}(m_1, m_2, z_m)$ has been integrated over all merger parameters λ except m_1 , m_2 , and merger redshift for merger type α . T_{obs} is the time that at least two detectors were running during a particular gravitational-wave observing run.

| Series | Parameters Varied (Λ) | Supernova Engine |
|---------|---|---------------------------------|
| M | Many Parameters Varied | Varied |
| M13-M19 | σ_{kick} | Rapid (strong pair-instability) |
| R | $f_a, \beta, \sigma_{\text{kick}}$ | Rapid (weak pair-instability) |
| D | $f_a, \beta, \sigma_{\text{kick}}, f_{\text{wind1}} = f_{\text{wind2}}$ | Delayed (weak pair-instability) |

Table 3.1:

Families of StarTrack synthetic universes included in this dissertation. Note that M-series models are the same as those that appear in Belczynski et al. (2020) [28].

| Model | σ_{kick} (km/s) |
|-------|-------------------------------|
| M13 | 265 |
| M14 | 200 |
| M15 | 130 |
| M16 | 70 |
| M17 | 35 |
| M18 | 20 |
| M19 | 10 |

Table 3.2: The σ_{kick} velocity is varied for the M13-M19 models.

3.4 Simulation Properties

Now we discuss the properties of the StarTrack synthetic universes included in this study. We consider several families of models (see table 3.1), with different assumptions about the formation parameters for binary evolution (Λ). The primary formation parameters varied in each simulation include: supernova recoil kick velocity applied to compact objects after a supernova explosion (σ_{kick}), two parameters characterizing ejected mass and mass transfer (f_a and β), and the mass loss from common envelope evolution due to stellar wind, (f_{wind1}). We also consider rapid and delayed supernova engines with varying assumptions about pair-instability. For each of these synthetic universes, we estimate the merger rate density $\rho_{\Lambda}(\lambda)$ and detection rate density $\mathcal{R}_{\Lambda}(\lambda)$ for the entire population (see sections 3.3.1 and 3.3.2). A full Bayesian comparison of the predicted gravitational-wave detection rate for each model to real observations is the focus of the next chapter. In advance of this, we are interested in exploring these properties of the merger population representing each model.

3.4.1 Initial Models

The first set of models we study are those from Belczynski et al. (2016), which are labeled consistently with that study (M10, M15, etc...) [25]. The only exception is M19, which hasn't been presented before. We refer to these as the M-series models, and these models explore a large dimensional parameter space, effectively narrowing

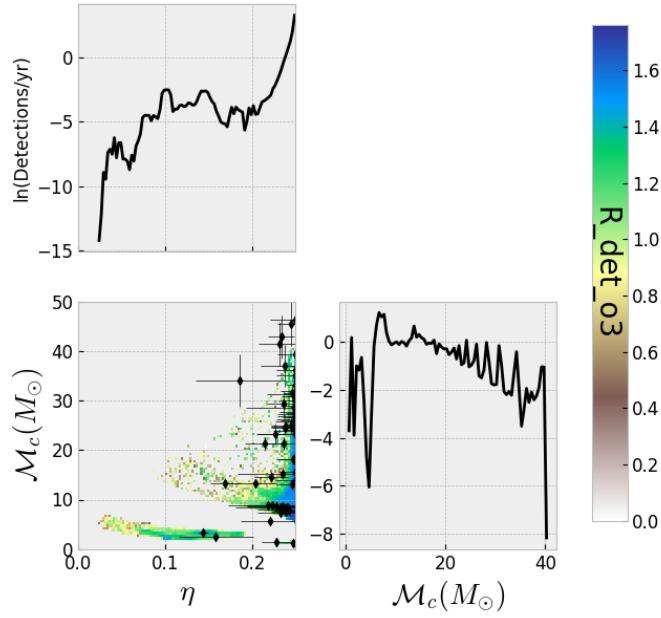


Figure 3.1: Detection-rate weighted histograms for the sample mergers in the M15 StarTrack synthetic universe. Diagonal elements indicate one-dimensional histograms (log base e), while the off-diagonal element shows a two-dimensional histogram (where color indicates the detection rate (yr^{-1}) for each bin; log base e). MLE estimates for real gravitational-wave events included in our study are indicated by black diamonds, with error bars representing the characteristic σ associated with NAL models for each event.

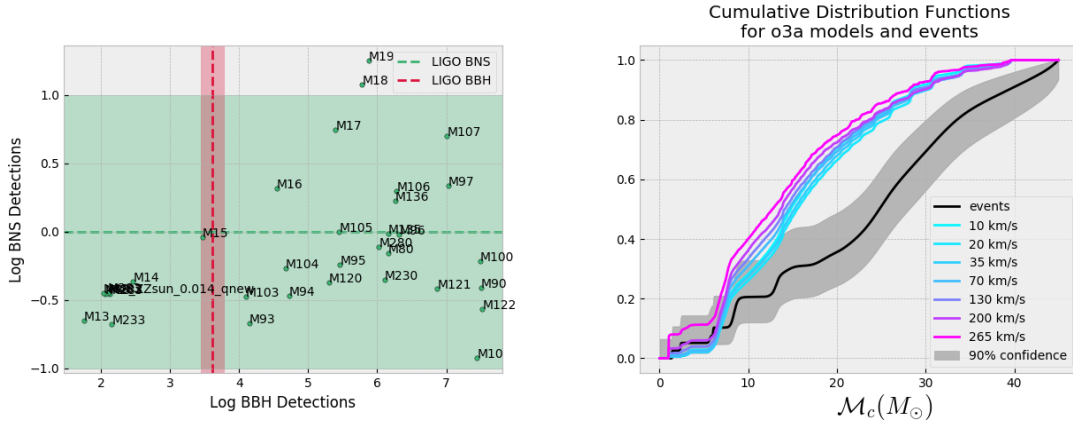


Figure 3.2: Detection rates for the limited M-series are compared to the first part of the third observing run (GWTC-2). (left) The detection rates predicted (log base e) for binary black holes and neutron stars are labeled for individual StarTrack models in this scatter plot. The dotted lines represent the number of observed detections for a given kind in GWTC-2, and shaded regions indicate Poisson counting error. (right) CDFs in source-frame chirp mass \mathcal{M}_c (similar to figure 2.7). Thin colored lines demonstrate the predicted gravitational-wave events in the M-series population models, (colored by σ_{kick}). The shaded region represents a 90% symmetric credible Wilson score interval [202].

down our search for the ideal set of parameters. Within the M-series, the M13-M19 models hold all formation parameters constant except for the supernova recoil kick velocity associated with BBH mergers, σ_{kick} (section 3.2.3), which is varied between 10 – 265 km/s (see table 3.2). This subset of the M-series models holds $f_a = 0.5$, $\beta = 1.0$, and $f_{\text{wind}1} = 1.0$. These M-series models feature a rapid supernova engine with strong PPSN/PSN. [28, 127].

We take a closer look at one of these models (M15) in particular, to describe the properties of a simulation before drawing an inference in the larger parameter space. The cosmological merger rates represent a density in merger parameters $\rho_{\Lambda}(\lambda)$, for a population representing one set of formation parameters, Λ . We see the detection rate as a function of source parameters (\mathcal{M}_c and η). For each merger in the simulation for M15, the detection rate is estimated as in eq. 3.10. Therefore, figure 3.1 represents not simply the density of sample mergers in a synthetic universe predicted by M15, but the density of those mergers which would be detected by a gravitational-wave observatory in such a universe.

The M15 model is a good fit to the observed detection rate (see fig 3.2; left panel). The substantial mass gap present for this model is indicative of the rapid supernova engine. This model is able to produce most events observed by the collaboration, but fails to describe mass gap events and under-predicts high mass events.

Trends in the observed detection rate for M-series models can be seen in figure

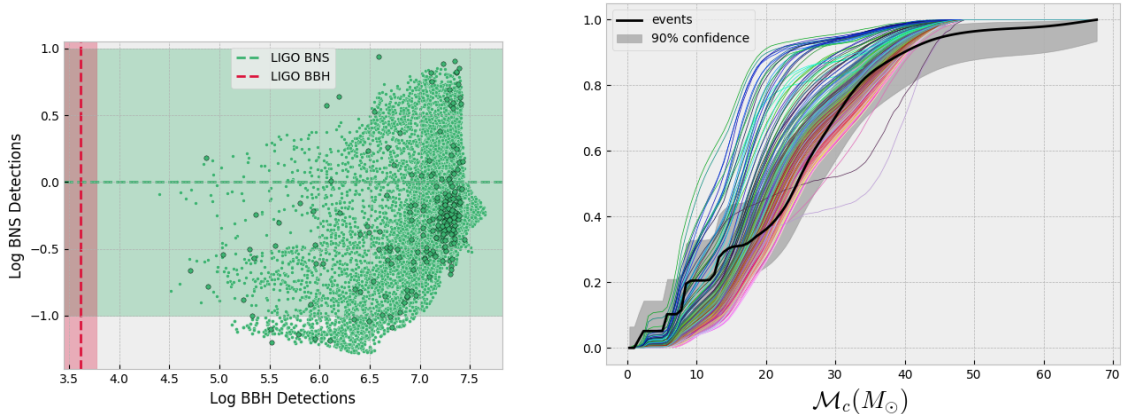


Figure 3.3: Detection rates for the R-series are compared to the first part of the third observing run (GWTC-2). Structurally similar to figure 3.2. (left) The smaller points are drawn from interpolated models of the larger parameter space of the R series simulations. (right) The color scale for R-series model CDFs encode the three formation parameters as Red, Green, and Blue values for f_a , β , and σ_{kick} . For the R-series models, we study a wider mass range than before, with the goal of reproducing the more massive BBH mergers observed in the third observing run.

3.2. The scatter plot compares the predicted binary black hole event rates and binary neutron star event rates for population models in the M series. The CDF plot compares the shape of each detection-weighted sample density in each StarTrack synthetic universe. In the next chapter (sec 4.2), we will examine how well the properties of these detection rate predictions agree with the observations reported in the GWTCs.

3.4.2 Preliminary Uniform Parameter Space

Following the one-dimensional study, the R-series models explore a formation parameter space given by 300 randomly sampled points in the space of f_a , β , σ_{kick} , with a rapid supernova engine, fixed $f_{\text{wind1}} = 0.2$, and weak pair-instability. f_a is varied between 0 and 1. β is varied between 0 and 1. σ_{kick} is varied between 0 and 265 km/s. The reduced mass loss due to stellar wind was expected to assist in producing high mass events such as the observed event, GW190521, through isolated binary evolution alone. However, as seen in figure 3.3, the R-series models overpredict gravitational-wave detection rates by several orders of magnitude. These detection rates lead us to believe that some of our assumptions in the formation parameters of these models may have been wrong. This is explored in greater detail in section 4.3.

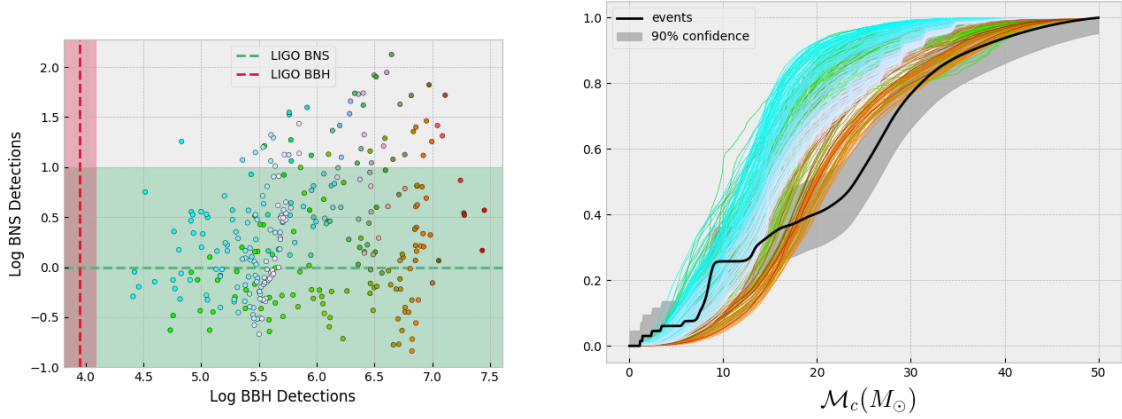


Figure 3.4: Structurally similar to figure 3.2. (left) Detection rates for the D-series are compared to the third observing run of (GWTC-2 and GWTC-3). (right) Detection rate CDFs for the D-series models are shown for comparison with all events for the first three observing runs (colored by an RGB scale in f_a , the detection rate log likelihood; e.g. eq 4.4, and $f_{\text{wind}1}$). For the D-series mergers, our mass range highlights most of the high-mass systems observed in LIGO/Virgo’s third observing run, however our binary evolution simulations do not result in any mergers like GW190521.

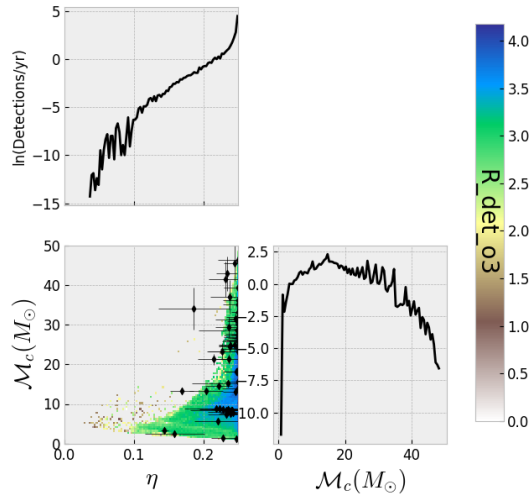


Figure 3.5: Detection-rate weighted histograms for the sample mergers in the and D411 StarTrack synthetic universe (log base e), in the style of figure 3.1.

3.4.3 Delayed Supernova Engine and Wind

Following our studies in the one- and three- formation parameter spaces of the M- and R-series synthetic universes, the properties of those models convinced us (see section 4.3) to explore the formation parameter f_{wind1} as well, with an updated delayed supernova engine and weak pair-instability, consistent with Belczynski et al. (2020) [28, 127]. The formation parameter space for the D-series synthetic universe models is uniformly distributed in f_a , β , and σ_{kick} like the R-series models (but with $0 < f_a < 0.25$). Of the 300 models generated for this series, 100 models are held at fixed $f_{\text{wind1}} = 0.2$, 100 models at fixed $f_{\text{wind1}} = 1.0$, and 100 models varied uniformly in f_{wind1} between those values. We note that the detection rate found for these models is more consistent with observations than the R-series models, and a full likelihood analysis follows in section 4.3.

We include figure 3.5, which shows the difference in the predicted population of gravitational-wave detections with a delayed supernova engine. Notice the lack of a substantial mass gap, compared to M15 (fig 3.1). For the delayed engine models, the D411 synthetic universe is our best match to observations (see chapter 4), with $f_a = 0.0185$, $\beta = 0.94$, $\sigma_{\text{kick}} = 205\text{km/s}$, and $f_{\text{wind1}} = 1.0$.

Chapter 4

Population Synthesis

The previous chapter demonstrated our procedure for estimating sample merger densities for massive binaries in synthetic universes generated with the StarTrack population synthesis models for a choice of formation parameters $\rho_\Lambda(\lambda)$. We have also explored the properties of these merger populations, including the predicted gravitational-wave detection rates. Now we explore the Bayesian population inference framework that allows us to constrain these binary evolution processes in a space of these formation parameters. This analysis is built upon the Bayesian framework described by other groups such as Dominik et al. and Wysocki et al. [69, 207, 208]. We study a one-, three-, and four-dimensional parameter space of StarTrack population synthesis models, and use these simulations to constrain the evolution of massive stellar binaries. These results draw heavily upon my forthcoming publication which has been presented internally to the LSC in 2020 and presented at the American Physical Society’s April meeting in 2021.

4.1 Bayesian Population Inference

The observation of gravitational-wave events can be modeled as an Inhomogeneous Poisson Point Process [208]. This representation allows us to evaluate the probability of the set of observed detections in the GWTC releases, $\{d_j\}$, for a simulated merger population, $\rho_\Lambda(\lambda)$. We must evaluate the relative likelihood that a population model accurately describes the detections observed by gravitational-wave detectors. This quantity, $P(\{d_j\}|\Lambda)$, equivalent to calculations done by others in the field [208, 188], can be decomposed as such:

$$P(\{d_j\}|\Lambda) = P(\mu|\Lambda) \prod_j P(d_j|\Lambda) \tag{4.1}$$

where the agreement of the predicted detection rate, μ , for a synthetic universe described by the formation parameters, Λ , with the observed detection rate in the GWTC releases for each type of event (E.g. BBH, BNS, NSBH) are described by simple Poisson Point Process components, and contained in the “rate likelihood” $P(\mu|\Lambda)$. Meanwhile, the agreement of the properties of sample mergers in that synthetic universe with the likelihood function attributed to the parameters of each real gravitational-wave detection is contained in “shape likelihood” $P(d_j|\Lambda)$.

We make use of Gaussian Process regression in order to interpolate these results, so as to describe the parameter space between simulations. The interpolation is carried out using the `gp-api` software package developed by our group (see section 2.1.1), using a kernel with piecewise polynomial basis functions with compact support, as outlined in Williams and Rasmussen [201]. The scale coefficient hyperparameters for the kernel are chosen by hand for the interpolations carried out in this chapter.

4.1.1 Detection Rate Likelihood

We have previously calculated these detection rates, $\mathcal{R}_{\Lambda,\alpha}$, and predicted number of detections, $\mu_{\Lambda,\alpha}$, for each of the population models described in section 3.4 (see eq. 3.12). The observation time, T_{obs} , assumed is consistent with GWTC release estimates for the time at least 2 detectors were running. The probability of an observed number of detections for a given type of event ($\alpha \in \{\text{BBH}, \text{BNS}, \text{NSBH}\}$), is dependent on the predicted rate for each type of event, described by the Poisson Point Process:

$$P(\mu_\alpha|\Lambda) = e^{-(\mathcal{R}_{\Lambda,\alpha}T_{\text{obs}})} \frac{(\mathcal{R}_{\Lambda,\alpha}T_{\text{obs}})^{N_\alpha}}{N_\alpha!} \quad (4.2)$$

where N_α is the number of gravitational-wave detections of type α reported in the GWTCs. Alternatively, the log rate likelihood is

$$\ln(P(\mu_\alpha|\Lambda)) = -(\mathcal{R}_{\Lambda,\alpha}T_{\text{obs}}) + N_\alpha \ln(\mathcal{R}_{\Lambda,\alpha}) + N_\alpha \ln(T_{\text{obs}}) - \ln(N_\alpha!) \quad (4.3)$$

where the last two terms do not depend on the properties of the synthetic universe, Λ , and can be ignored to a factor of renormalization.

The total combined rate likelihood is therefore

$$P(\mu|\Lambda) = \prod_\alpha \left[\frac{(\mathcal{R}_{\Lambda,\alpha}T_{\text{obs}})^{N_\alpha}}{N_\alpha!} \right] e^{-\sum_\alpha \mu_{\Lambda,\alpha}} = \mathcal{K}_{\text{rate}} e^{-\mu_\Lambda} \quad (4.4)$$

Or alternatively,

$$\ln(P(\mu|\Lambda)) \propto \sum_\alpha (-\mathcal{R}_{\Lambda,\alpha}T_{\text{obs}} + N_\alpha \ln(\mathcal{R}_{\Lambda,\alpha})) = -\mu_\Lambda + \sum_\alpha N_\alpha \ln(\mathcal{R}_{\Lambda,\alpha}) \quad (4.5)$$

4.1.2 Shape Likelihood

The agreement of the sample mergers in a StarTrack synthetic universe with the properties of the gravitational-wave signals observed thus far by gravitational-wave detectors is measured by the Inhomogeneous Poisson likelihood, as stated above. The “shape likelihood” is the contribution toward this likelihood from the shape of the distribution of observed detections. This quantity measures the agreement of the sample merger density, $\rho_\Lambda(\lambda)$, for a synthetic universe (represented by some formation parameters, Λ) with the likelihood for the astrophysical parameters of each gravitational-wave detection, $\mathcal{L}_j(\lambda)$. This quantity is marginalized (integrated) over the entire population of sample mergers in a synthetic universe:

$$P(d_j|\Lambda) = \int_{\lambda} P(d_j|\lambda, \Lambda)P(\lambda|\Lambda)d\lambda = \int_{\lambda} \bar{\rho}_\Lambda(\lambda)\mathcal{L}_j(\lambda)d\lambda \quad (4.6)$$

where $\bar{\rho}_\Lambda(\lambda) = \rho_\Lambda(\lambda)/\int_{\lambda'} \rho_\Lambda(\lambda')d\lambda'$.

The marginalization is carried out over the entire population of 10^8 sample compact binary mergers in a each synthetic universe, for each gravitational-wave observation from a given observing run. In this chapter, we consider the likelihood contribution from the same events included in the LSC’s O3 rates and populations paper [51], with the exclusion of GW190521, which we expect may be inconsistent with isolated binary evolution (see sec 4.3). The discrete evaluation would not be computationally reasonable without an approximate model for each likelihood that can be evaluated in a small fraction of second. We make use of the NAL estimates provided in chapter 2 for this integration.

4.1.3 Joint Likelihood

Our complete expression for the joint likelihood agrees with Wysocki et al. 2019 [208]:

$$P(\{d_j\}|\Lambda) \propto K_{\text{rate},i}e^{-\mu} \prod_j \left[\int_{\lambda} \bar{\rho}(\lambda)\mathcal{L}_j(\lambda)d\lambda \right] \quad (4.7)$$

Alternatively the logarithmic representation:

$$\ln(P(\{d_j\}|\Lambda)) \propto -\mu_\Lambda + \sum_{\alpha} [N_{\alpha}\mathcal{R}_{\Lambda,\alpha}] + \sum_j \left[\int_{\lambda} \bar{\rho}(\lambda)\mathcal{L}_j(\lambda)d\lambda \right] \quad (4.8)$$

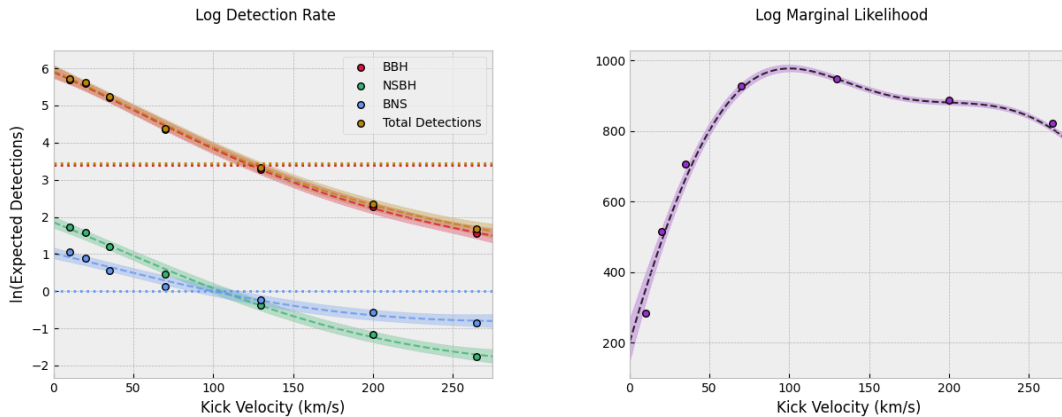


Figure 4.1: Detection rates (left) and the joint likelihood (right) for various gravitational-wave events as function of the kick velocity formation parameter. Scatter points indicate model simulations (M13-M19). The dashed curve indicates the mean from a Gaussian process regression interpolation. For this example only, scikit-learn is used for the interpolation due to the small number of training points. The shaded region is of one standard deviation error from that Gaussian process. The dotted line (left) indicates the published number of detections for the first part of the LIGO’s third observing run. There is a clear peak in likelihood near M15, where the kick velocity is 130 km/s, and where the LIGO detection rates also agree.

4.2 Kick Velocity; A One-Dimensional Study

The M-series models shown in figure 3.2 include many families of cosmological formation parameters Λ . In our first one-dimensional study, we limit ourselves to the models M13-M19, which hold everything constant except σ_{kick} which varies from 10 km/s to 265 km/s (see sec 3.4.1). We note that the contribution from individual events (shape likelihood) dominates the joint likelihood for this family of models, changing more rapidly between populations than the rate likelihood. As seen in figures 3.2 and 4.1, we see the best agreement with model M15, with $\sigma = 130\text{km/s}$. and our analysis are in favor of modest supernova recoil kicks for black holes.

In the space of the kick velocity formation parameter, we have generated an interpolation using a Gaussian Process Regression algorithm. The Gaussian process helps to describe the detection rate for each type of event in the space between simulations. It also describes the joint likelihood in that space. We find that a modest kick velocity is appropriate for our model of binary evolution.

4.3 Higher-Dimensional Studies: $f_a, \beta, \sigma_{\text{kick}}, f_{\text{wind}1}$

Following the one-dimensional investigation, the next set of models we study is a three-dimensional formation parameter space, constraining f_a, β , and σ_{kick} using an updated

rapid supernova engine. As seen in section 3.4.2 (figure 3.3), the R-series models do not predict similar detection rates to the one-dimensional M-series study and are inconsistent with observation. This can be explained by differences in the supernova engine, together with differences in the mass loss due to stellar wind, f_{wind1} . Unfortunately, the decreased mass loss due to stellar winds assumed in the R-series models predicts an overabundance of binary black hole detections for this set of models by several orders of magnitude. For these models, the inconsistency with the observed gravitational-wave detection rate dominates likelihood calculation (the rate likelihood contribution; see fig 4.2).

In hindsight, the choice of $f_{\text{wind1}} = 0.2$ for these models proved to be an optimistic attempt to produce events such as GW190521 by isolated binary evolution. Recent studies have argued GW190521 has properties (such as orbital eccentricity at time of merger) which are not consistent with isolated binary evolution, and may be the result of a dynamic (3 or more bodies) merger [83, 81, 170]. In light of this, and because it is unreasonable to expect that all of the marginal detections reported in GWTC-2.1 are of astrophysical origin [52], we must not demand that our StarTrack synthetic universe can predict every single merger reported in the GWTC releases. Doing so may over-constrain the parameters of the isolated binary evolution channel to produce unrealistic results.

Finally, we have also generated a tertiary set of merger populations varying the same three parameters, using a delayed supernova engine, and also varying the factor of reduced mass loss, f_{wind1} assumed by contemporary literature [28]. The D-series models provide more compelling constraints on the astrophysical assumptions about binary evolution encoded in these parameters.

4.3.1 The Delayed Supernova Engine

Before exploring the four-dimensional parameter space composing the D-series models, we take a moment to consider the same three-dimensional parameter space explored previously by the R-series. The first 100 models in the D-series keep a fixed value of $f_{\text{wind1}} = 0.2$, consistent with the R-series models. Therefore, it is worth drawing a comparison between the R-series models and this reduced set of D-series models in order to characterize the effect of changing the supernova engine (see fig 4.2).

For both sets of models, we find a high correlation between the estimated detection rate and our f_a formation parameter, however this effect is less prominent for the delayed supernova engine. Rather than drawing strong conclusions about the f_a parameter based on this correlation, we note that even for low f_a , we still predict an overabundance of BBH detections (see fig 3.3 and 3.4). It is worth considering what kind of biases we may be introducing to our estimation of the predicted detection rates due to our detection model.

We use a Gaussian process between models to predict the detection rate likelihood in the entire parameter space studied in each series of models (3.4.2, 3.4.3). This method allows us to study a larger formation parameter space without an ever-increasing num-

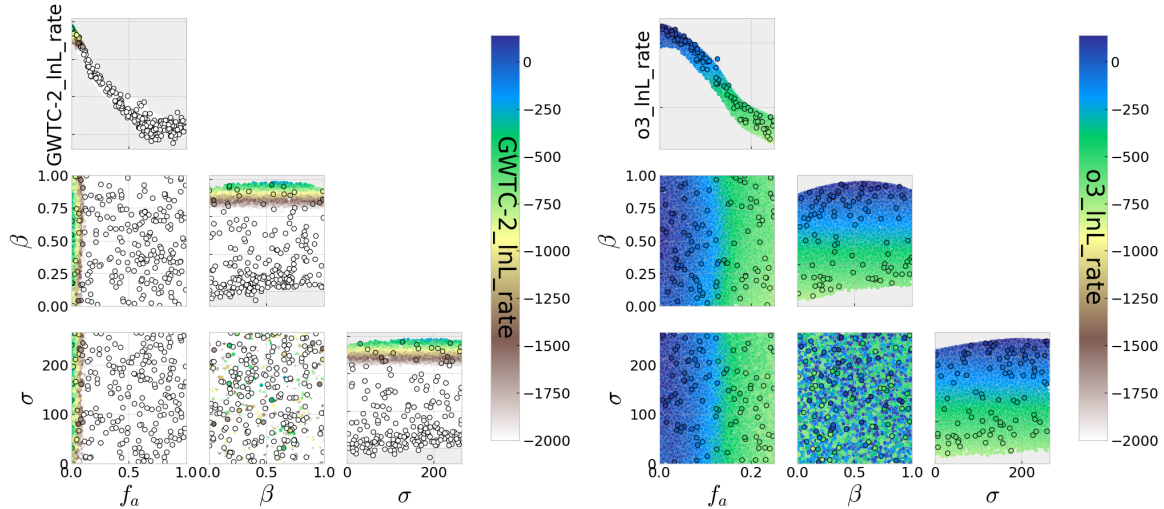


Figure 4.2:

Scatter plots highlight the relative probability with which synthetic universes with formation parameters varied in f_a , β , and σ_{kick} represent a realistic model, based on solely the detection rate likelihood in log scale (colorbar) (eq 4.4, 4.5). Each synthetic universe for the R-series models (left), and the subset of D-series models with $f_{\text{wind1}} = 0.2$ (right) are represented by a point with a black border. A Gaussian process regression interpolation is used to estimate the rate likelihood between synthetic universe models (smaller points with white borders). Note the difference in scale in f_a . We consider the first part of the third observing run for R-series models, and the entire third observing run for D-series models. We observe that synthetic universes with both supernova engines over-produce observable BBH events, which necessarily constrains f_a to be small, due to the high correlation between f_a and detection rates at low f_{wind1} . However, this overabundance is scaled down with the delayed engine supernova model.

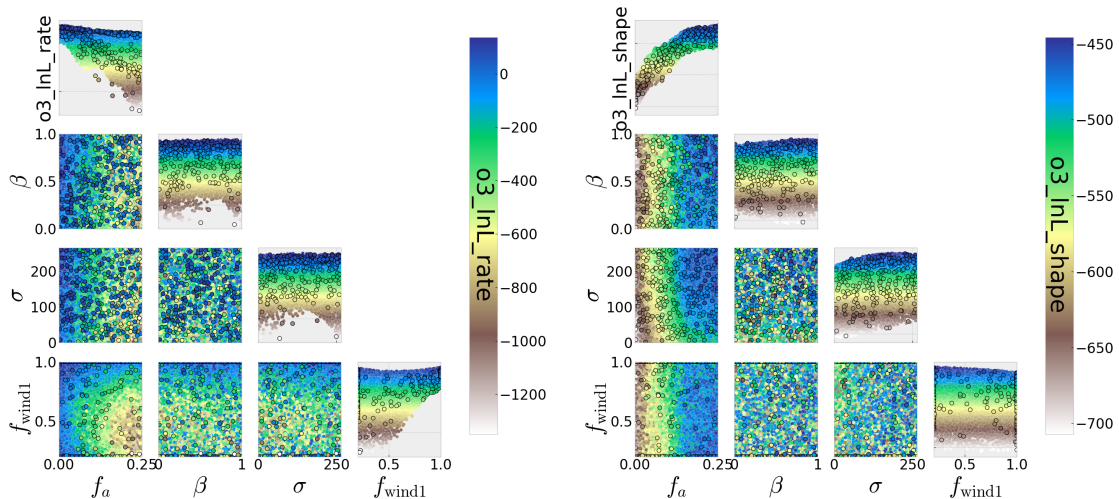


Figure 4.3: The shape likelihood (left) and rate likelihood (right) for the full set of D-series synthetic universe models, using the same style as fig 4.2 (log base e; see eq 4.5, 4.6). Note that at high f_{wind1} , the correlation between rate likelihood and f_a is reduced. Note also that the shape likelihood favors $f_a > 0$.

ber of simulations. We use our own Gaussian process regression algorithm for this application (sec 2.1.1).

4.3.2 Constraints on Isolated Binary Evolution in Four Dimensions

At last, we can use the full set of delayed supernova engine models to constrain the formation parameters of our StarTrack synthetic universe formula (see sec 3.4.3). We show the (log base e) likelihood for each synthetic universe in figures 4.3 and 4.4, featuring scatter-plots and Gaussian process interpolations for the rate likelihood, shape likelihood, and joint likelihood (sec 4.1). We explore the implications of different choices for the formation parameters f_a , β , σ_{kick} , and f_{wind1} on these quantities, and in doing so demonstrate our method for constraining these processes in the isolated binary evolution formation channel for gravitational-wave events.

Our method allows us to assess the quality of fit between each synthetic universe and the observed gravitational-wave population by separately evaluating the agreement in detection rate and the shape of the population. This gives us the ability to study the dependence of the rate and shape likelihood components on the formation model independently. When the rate and shape likelihood disagree, this gives us cause to re-examine our formation model. When these quantities are in agreement the joint likelihood will be maximized, indicating the best potential candidate for a realistic set of formation model assumptions.

While the joint likelihood for the M-series models was strongly constrained by the

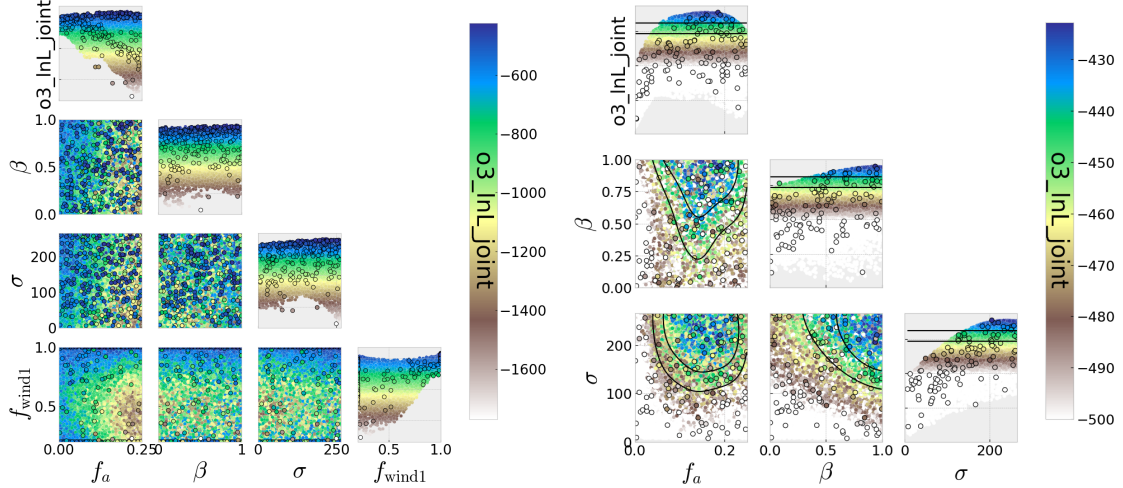


Figure 4.4: The joint likelihood (log base e; see eq 4.8) for models in the D-series, in the same style as fig 4.2. (left) the full set of models in four dimensions. (right) a three-dimensional interpolation of only high wind models with horizontal lines and contours for regions of 1 and 2 σ in the Gaussian process estimated uncertainty.

| Model | $\ln\mathcal{L}_{\text{joint}}$ | $\ln\mathcal{L}_{\text{rate}}$ | $\ln\mathcal{L}_{\text{shape}}$ | f_a | β | σ_{kick} (km/s) | f_{wind1} |
|-------|---------------------------------|--------------------------------|---------------------------------|-------|---------|-------------------------------|--------------------|
| D411 | 0.000 | -98.149 | -16.107 | 0.185 | 0.938 | 205.624 | 1.00 |
| D473 | -3.539 | -98.715 | -19.079 | 0.190 | 0.954 | 220.655 | 1.00 |
| D301 | -3.906 | -96.591 | -21.571 | 0.160 | 0.792 | 211.110 | 1.00 |
| D407 | -7.924 | -75.311 | -46.868 | 0.122 | 0.566 | 257.617 | 1.00 |
| D465 | -8.619 | -97.120 | -25.755 | 0.155 | 0.887 | 183.200 | 1.00 |
| D426 | -101.096 | 0.000 | -215.351 | 0.010 | 0.594 | 236.519 | 1.00 |
| D027 | -628.026 | -742.282 | 0.000 | 0.249 | 0.683 | 226.504 | 0.20 |

Table 4.1: Quantities of interest for the simulations with the five best joint likelihood estimates, the best rate likelihood estimate, and the best shape likelihood estimate. Tabulated values are re-scaled by the by the highest likelihood for each category ($\ln\mathcal{L}_{\text{joint-max}} = -422.824$, $\ln\mathcal{L}_{\text{rate-max}} = 136.966$, $\ln\mathcal{L}_{\text{shape-max}} = -445.534$).

shape of the population, and the joint likelihood of the R-series models was dominated by the effect of the detection rate, we observe that with the delayed supernova engine, the rate likelihood and shape likelihood contributions are at similar orders of magnitude, and both contribute to the joint likelihood. We observe a relative agreement from these models in some formation parameters. The rate and shape likelihoods both support substantial supernova kicks, consistent with our M-series models. We see also a tendency towards high β in both likelihood estimates.

We also observe a strong codependence of the predicted detection rates on both mass loss rate due to stellar wind (f_{wind1}) and f_a . However, the rate and shape likelihood are in disagreement in their predictions about f_a , with the shape likelihood predicting a modest $f_a > 0$. This is an indication that we may need to re-examine our detection model.

In the above work, we have methodically examined our use of the Inhomogeneous Poisson Point Process to identify potential systematic bias in our model (for example, we consider potential bias in a mis-tuned detection model as well as an incomplete exploration of model parameter spaces). However, the final analysis of our likelihood model does demonstrate a peak in a consistent region of parameter space. Keeping in mind the sources of bias we have discussed, we characterize the preferred model parameters. As seen in figure 4.4, we see a peak in likelihood at $f_{\text{wind1}} = 1$. This is further explored by considering the three-dimensional set of models where $f_{\text{wind1}} = 1$ is constant. The properties of the models which best match observation are given in table 4.1, including our preferred model, D411. The estimated uncertainty in our parameters for the models in the vicinity of parameter space with highest joint likelihood are generated by the Gaussian process, and regions of one- and two-sigma are observed in figure 4.4.

Chapter 5

Conclusions

Throughout this dissertation I have introduced methods, demonstrated application, and shared our findings in modeling the properties of individual gravitational-wave events, and constraining population models for the isolated binary evolution formation channel for compact binaries. In this final chapter, I provide a summary of our methods and results, and I present our conclusions. Furthermore, I discuss the broader impact of my work on parameter estimation, population synthesis, and the field of multi-messenger astronomy.

5.1 Summary

We present both compressed parametric and non-parametric methods for fully characterizing the astrophysical properties of each gravitational-wave event reported by modern gravitational-wave observatories. We have demonstrated that our method is versatile and applicable to high-dimensional parameter spaces, including source-frame or detector-frame mass parameterizations, distance, precessing spin, and the tidal deformability of neutron stars. We use these methods to also provide optimized parameterizations for the bounded (truncated) Normal Approximate Likelihood (NAL) models describing each event reported in the Gravitational-Wave Transient Catalogs. Each NAL model has the added benefit of describing a maximum likelihood estimate for the properties of a given event which is unbiased by the finite boundary limitations imposed by similar models assumed from the sample mean.

We find that NAL models are in strong agreement with the parameter estimation sample density for events in the GWTC releases, even for a selection of sparsely simulated likelihood evaluations. These models can be used to compare the properties of the gravitational-wave population to any population model (including popular Monte Carlo methods), due to their accuracy and computational efficiency. Furthermore, their less biased maximum likelihood estimates for the parameters of each event can be syn-

thesized to describe the bulk properties of the population on an event-by-event basis, such as the mass distribution and tendency toward equal mass in compact binaries. The characteristic σ associated with the optimized truncated Gaussian also provides an excellent standard for describing the half-width-half-max of a truncated Gaussian and the significance of a deviation from equal mass and zero (or liminal) spin. Our findings are also in agreement with collaborative works, in that populations of compact binaries observed by modern gravitational-wave detectors have mostly equal mass and zero spin (with notable exceptions).

Following this, we use the StarTrack binary evolution algorithm to construct synthetic universes representing a population of merging binaries under a range of assumptions about the underlying parameters of binary evolution. Using these populations, we apply a detection model to predict the rate of gravitational-wave observations and compare those predicted observations to those reported by real gravitational-wave observatories. We apply Bayesian statistical inference to compare both the predicted detection rates and properties of predicted compact binaries to real observations reported by gravitational-wave observatories. We extend our analysis using Gaussian process regression to consider the parameter space between simulations, fully characterizing a response in our range of allowed values for each formation parameter. We provide our method for this analysis, as well as our conclusions about the impact of formation parameters on the isolated binary evolution formation channel.

With our simplified detection model, we demonstrate the effectiveness of our methods as we draw preliminary constraints on four formation parameters (f_a , β , σ_{kick} , and f_{wind1}) for the isolated binary evolution formation channel. Our analysis includes efficient techniques for comparing a large discrete set of population models to gravitational-wave observations, an interpolation model which can predict around those discrete models, as well as systematic consistency tests which check if each component of our model is in agreement. We find that both f_a and f_{wind1} have a strong impact on the gravitational-wave detection rate associated with a binary evolution model. These parameters, together with the supernova engine assumed for the isolated binary evolution formation channel, must both be considered when analyzing the agreement of the detection rate predicted for a simulated merger population to real observations. Presently, our results suggest an unrestricted stellar mass loss due to wind, as well as substantial supernova recoil kicks, and significant mass and angular momentum loss due to ejected material during the common envelope phase of binary evolution (see sec 4.3.2).

5.2 Broader Impacts of Science and Methodology

The significance of this work has immediate consequences for related studies in the field of multi-messenger astronomy. As many groups are interested in studying the formation channels of compact binary mergers, quickly assessing the agreement of sample mergers to the real gravitational-wave events reported in the GWTC releases is of immediate application. NAL models provide this application and are available as

a public release (<https://gitlab.com/xevra/nal-data>), together with our methods (<https://gitlab.com/xevra/gwalk> and <https://gitlab.com/xevra/gp-api>). As gravitational-wave detectors move closer to design performance in future observing runs, inefficient sample-based estimates for the likelihood function of each gravitational-wave event for a population model will become increasingly computationally challenging. NAL models can be used to fully characterize the astrophysical properties of each merger and can be evaluated in a small fraction of a second (even for high-dimensional parameter spaces), and will be ever more useful in upcoming observing runs for efficient population synthesis.

Conclusions about the formation parameters for the isolated binary evolution channel for the formation of compact binaries are also of immediate consequence to other work. Our results can inform other population synthesis models of reasonable expectations for the physical processes in binary evolution, and what assumptions are valid to make. More widely in multi-messenger astronomy, a simulated synthetic universe with predicted compact binary detection rates in agreement with gravitational-wave observations will help to predict other physics by providing physically motivated sets of sample mergers representing stellar populations. One example of these broader applications includes work done by my colleague, using our population synthesis model to constrain the neutron star equation of state [97].

Even directly, as our detection model, population of gravitational-wave signals, and simulation sample expand, we can further constrain our formation channel. This will allow us to fit an even wider set of models for mass transfer in binary systems, mass loss due to stellar wind in stars with varying mass and metallicity, as well as supernova engines and ejecta. Future work can further strengthen these constraints by considering the agreement of stellar populations predicted in these synthetic universes with multi-messenger observation, such as Gaia populations and electromagnetic neutron-star emission, and by considering dynamic mergers as other groups have proposed [176]. Such an analysis can fully apply the potential of multi-messenger astrophysics to form a more complete understanding of stellar populations and evolution in our Universe.

Bibliography

- [1] J. Aasi, J. Abadie, B. P. Abbott, R. Abbott, and et al. FIRST SEARCHES FOR OPTICAL COUNTERPARTS TO GRAVITATIONAL-WAVE CANDIDATE EVENTS. *The Astrophysical Journal Supplement Series*, 211(1):7, feb 2014.
- [2] B. Abbott, R. Abbott, T. Abbott, M. Abernathy, and et al. Directly comparing gw150914 with numerical solutions of einstein’s equations for binary black hole coalescence. *Physical Review D*, 94(6), Sep 2016.
- [3] B. Abbott, R. Abbott, T. Abbott, M. Abernathy, and et al. Gw150914: First results from the search for binary black hole coalescence with advanced ligo. *Physical Review D*, 93(12), Jun 2016.
- [4] B. Abbott, R. Abbott, T. Abbott, S. Abraham, and et al. Gwtc-1: a gravitational-wave transient catalog of compact binary mergers observed by ligo and virgo during the first and second observing runs. *Physical Review X*, 9(3):031040, 2019.
- [5] B. P. Abbott, R. Abbott, T. Abbott, F. Acernese, and et al. Gw170817: observation of gravitational waves from a binary neutron star inspiral. *Physical review letters*, 119(16):161101, 2017.
- [6] B. P. Abbott, R. Abbott, T. D. Abbott, S. Abraham, and et al. Binary black hole population properties inferred from the first and second observing runs of advanced ligo and advanced virgo. *The Astrophysical Journal*, 882(2):L24, Sep 2019.
- [7] B. P. Abbott, R. Abbott, T. D. Abbott, S. Abraham, and et al. Gw190425: Observation of a compact binary coalescence with total mass 3.4 m. *The Astrophysical Journal Letters*, 892(1):L3, Mar 2020.
- [8] B. P. Abbott, R. Abbott, T. D. Abbott, S. Abraham, and et al. Prospects for observing and localizing gravitational-wave transients with advanced LIGO, advanced virgo and KAGRA. *Living Reviews in Relativity*, 23(1), sep 2020.
- [9] R. Abbott, T. Abbott, S. Abraham, F. Acernese, and et al. Gwtc-2: Compact binary coalescences observed by ligo and virgo during the first half of the third observing run. *Physical Review X*, 11(2):021053, 2021.

-
- [10] B. Abbott et al. (The LIGO Scientific Collaboration and the Virgo Collaboration). Astrophysical Implications of the Binary Black-hole Merger GW150914. *Astrophysical Journal*, 818:L22, Feb. 2016.
- [11] H. A. Abt. Normal and abnormal binary frequencies. *Annual Review of Astronomy and Astrophysics*, 21(1):343–372, 1983.
- [12] H. A. Abt and S. G. Levy. Binaries among B2 - B5 IV, V absorption and emission stars. *ApJS*, 36:241–258, Feb. 1978.
- [13] F. Acernese, M. Agathos, K. Agatsuma, D. Aisa, and et al. Advanced virgo: a second-generation interferometric gravitational wave detector. *Classical and Quantum Gravity*, 32(2):024001, dec 2014.
- [14] P. Ajith, M. Hannam, S. Husa, Y. Chen, B. Brügmann, N. Dorband, D. Müller, F. Ohme, D. Pollney, C. Reisswig, and et al. Inspiral-merger-ringdown waveforms for black-hole binaries with nonprecessing spins. *Physical Review Letters*, 106(24), Jun 2011.
- [15] J. M. Antognini, B. J. Shappee, T. A. Thompson, and P. Amaro-Seoane. Rapid eccentricity oscillations and the mergers of compact objects in hierarchical triples. *Monthly Notices of the Royal Astronomical Society*, 439(1):1079–1091, 02 2014.
- [16] F. Antonini, N. Murray, and S. Mikkola. BLACK HOLE TRIPLE DYNAMICS: A BREAK-DOWN OF THE ORBIT AVERAGE APPROXIMATION AND IMPLICATIONS FOR GRAVITATIONAL WAVE DETECTIONS. *The Astrophysical Journal*, 781(1):45, jan 2014.
- [17] G. Ashton, M. Hübner, P. D. Lasky, C. Talbot, K. Ackley, S. Biscoveanu, Q. Chu, A. Divakarla, P. J. Easter, B. Goncharov, F. H. Vivanco, J. Harms, M. E. Lower, G. D. Meadors, D. Melchor, E. Payne, M. D. Pitkin, J. Powell, N. Sarin, R. J. E. Smith, and E. Thrane. Bilby: A user-friendly bayesian inference library for gravitational-wave astronomy. *The Astrophysical Journal Supplement Series*, 241(2):27, apr 2019.
- [18] Y. Aso, Y. Michimura, K. Somiya, M. Ando, and et al. Interferometer design of the kagra gravitational wave detector. *Phys. Rev. D*, 88:043007, Aug 2013.
- [19] B. Aylott, J. G. Baker, W. D. Boggs, and M. B. et al. Testing gravitational-wave searches with numerical relativity waveforms: results from the first numerical INJection analysis (NINJA) project. *Classical and Quantum Gravity*, 26(16):165008, aug 2009.
- [20] M. Bailes. The Origin of Pulsar Velocities and the Velocity–Magnetic Moment Correlation. *Astrophysical Journal*, 342:917, July 1989.
- [21] I. Bartos, B. Kocsis, Z. Haiman, and S. Márka. Rapid and bright stellar-mass binary black hole mergers in active galactic nuclei. *The Astrophysical Journal*, 835(2):165, jan 2017.

-
- [22] N. Bastian, K. R. Covey, and M. R. Meyer. A universal stellar initial mass function? a critical look at variations. *Annual Review of Astronomy and Astrophysics*, 48(1):339–389, 2010.
- [23] T. Bayes. An essay towards solving a problem in the doctrine of chances. *Phil. Trans. of the Royal Soc. of London*, 53:370–418, 1763.
- [24] K. Belczynski, R. Hirschi, E. A. Kaiser, J. Liu, J. Casares, Y. Lu, R. O’Shaughnessy, A. Heger, S. Justham, and R. Soria. The Formation of a 70 M_{\odot} Black Hole at High Metallicity. *Astrophysical Journal*, 890(2):113, Feb. 2020.
- [25] K. Belczynski, D. E. Holz, T. Bulik, and R. O’Shaughnessy. The first gravitational-wave source from the isolated evolution of two stars in the 40–100 solar mass range. *Nature*, 534(7608):512–515, Jun 2016.
- [26] K. Belczynski, V. Kalogera, and T. Bulik. A comprehensive study of binary compact objects as gravitational wave sources: Evolutionary channels, rates, and physical properties. *The Astrophysical Journal*, 572(1):407–431, Jun 2002.
- [27] K. Belczynski, V. Kalogera, F. A. Rasio, R. E. Taam, A. Zezas, T. Bulik, T. J. Maccarone, and N. Ivanova. Compact object modeling with the startrack population synthesis code. *The Astrophysical Journal Supplement Series*, 174(1):223–260, Jan 2008.
- [28] K. Belczynski, J. Klencki, C. E. Fields, A. Olejak, and et al. Evolutionary roads leading to low effective spins, high black hole masses, and o1/o2 rates for ligo/virgo binary black holes. *Astronomy & Astrophysics*, 636:A104, Apr 2020.
- [29] K. Belczynski, S. Repetto, D. E. Holz, R. O’Shaughnessy, T. Bulik, E. Berti, C. Fryer, and M. Dominik. Compact binary merger rates: Comparison with ligo/virgo upper limits. *The Astrophysical Journal*, 819(2):108, Mar 2016.
- [30] K. Belczynski, A. Romagnolo, A. Olejak, J. Klencki, D. Chattopadhyay, S. Stevenson, M. C. Miller, J.-P. Lasota, and P. A. Crowther. The uncertain future of massive binaries obscures the origin of LIGO/virgo sources. *The Astrophysical Journal*, 925(1):69, jan 2022.
- [31] C. M. Biwer, C. D. Capano, S. De, M. Cabero, and et al. PyCBC Inference: A Python-based Parameter Estimation Toolkit for Compact Binary Coalescence Signal. *PASP*, 131(996):024503, Feb. 2019.
- [32] H. M. J. Boffin and A. Jorissen. Can a barium star be produced by wind accretion in a detached binary ? *A&A*, 205:155–163, Oct. 1988.
- [33] A. Bohé et al. Improved effective-one-body model of spinning, nonprecessing binary black holes for the era of gravitational-wave astrophysics with advanced detectors. *Phys. Rev. D*, 95(4):044028, 2017.
- [34] H. Bondi and F. Hoyle. On the mechanism of accretion by stars. *MNRAS*, 104:273, Jan. 1944.

-
- [35] M. Boyle, D. Hemberger, D. A. B. Iozzo, G. Lovelace, and et al. The SXS collaboration catalog of binary black hole simulations. *Classical and Quantum Gravity*, 36(19):195006, sep 2019.
- [36] K. Breivik, S. Coughlin, M. Zevin, C. L. Rodriguez, and et al. COSMIC variance in binary population synthesis. *The Astrophysical Journal*, 898(1):71, jul 2020.
- [37] K. Breivik, S. Coughlin, M. Zevin, C. L. Rodriguez, K. Kremer, C. S. Ye, J. J. Andrews, M. Kurkowski, M. C. Digman, S. L. Larson, and F. A. Rasio. COSMIC variance in binary population synthesis. *The Astrophysical Journal*, 898(1):71, jul 2020.
- [38] M. M. Briel, H. F. Stevance, and J. J. Eldridge. Understanding the high-mass binary black hole population from stable mass transfer and super-eddington accretion in bpass, 2022.
- [39] F. S. Broekgaarden and E. Berger. Formation of the first two black hole–neutron star mergers (gw200115 and gw200105) from isolated binary evolution. *The Astrophysical Journal Letters*, 920(1):L13, 2021.
- [40] F. S. Broekgaarden, E. Berger, S. Stevenson, S. Justham, I. Mandel, and M. Chruślińska. Impact of massive binary star and cosmic evolution on gravitational wave observations ii: Double compact object rates and properties. *arXiv preprint arXiv:2112.05763*, 2021.
- [41] I. Brott, S. E. de Mink, M. Cantiello, N. Langer, A. de Koter, C. J. Evans, I. Hunter, C. Trundle, and J. S. Vink. Rotating massive main-sequence stars. I. Grids of evolutionary models and isochrones. *A&A*, 530:A115, June 2011.
- [42] B. Brüggmann, J. A. González, M. Hannam, S. Husa, U. Sperhake, and W. Tichy. Calibration of moving puncture simulations. *Physical Review D*, 77(2), jan 2008.
- [43] T. A. Callister. A Thesaurus for Common Priors in Gravitational-Wave Astronomy. *arXiv e-prints*, page arXiv:2104.09508, Apr. 2021.
- [44] S. Chatterjee, W. H. T. Vlemmings, W. F. Brisken, T. J. W. Lazio, J. M. Cordes, W. M. Goss, S. E. Thorsett, E. B. Fomalont, A. G. Lyne, and M. Kramer. Getting its kicks: A VLBA parallax for the hyperfast pulsar b1508+55. *The Astrophysical Journal*, 630(1):L61–L64, aug 2005.
- [45] H. Cho, E. Ochsner, R. O’Shaughnessy, C. Kim, and C. Lee. Gravitational waves from BH-NS binaries: Phenomenological Fisher matrices and parameter estimation using higher harmonics. *Phys. Rev. D*, 87:02400–+, Jan. 2013.
- [46] H.-S. Cho, E. Ochsner, R. O’Shaughnessy, C. Kim, and C.-H. Lee. Gravitational waves from black hole-neutron star binaries: Effective fisher matrices and parameter estimation using higher harmonics. *Physical Review D*, 87(2), Jan 2013.
- [47] D. D. Clayton. *Principles of stellar evolution and nucleosynthesis*. Chicago: University of Chicago Press, 1983.

-
- [48] L. S. Collaboration and V. Collaboration. GWTC-2.1: Deep Extended Catalog of Compact Binary Coalescences Observed by LIGO and Virgo During the First Half of the Third Observing Run - Parameter Estimation Data Release, July 2021.
- [49] L. S. Collaboration, V. Collaboration, and K. Collaboration. GWTC-3: Compact Binary Coalescences Observed by LIGO and Virgo During the Second Part of the Third Observing Run — Parameter estimation data release, Nov. 2021.
- [50] T. L. S. Collaboration, the Virgo Collaboration, and the KAGRA Collaboration et al. Gwtc-3: Compact binary coalescences observed by ligo and virgo during the second part of the third observing run, 2021.
- [51] T. L. S. Collaboration, the Virgo Collaboration, and the KAGRA Collaboration et al. The population of merging compact binaries inferred using gravitational waves through gwtc-3, 2021.
- [52] T. L. S. Collaboration and the Virgo Collaboration et al. Gwtc-2.1: Deep extended catalog of compact binary coalescences observed by ligo and virgo during the first half of the third observing run, 2021.
- [53] J. M. Cordes and D. F. Chernoff. Neutron Star Population Dynamics. I. Millisecond Pulsars. *Astrophysical Journal*, 482(2):971–992, June 1997.
- [54] J. M. Cordes and D. F. Chernoff. Neutron Star Population Dynamics. II. Three-dimensional Space Velocities of Young Pulsars. *Astrophysical Journal*, 505(1):315–338, Sept. 1998.
- [55] N. J. Cornish. Fast fisher matrices and lazy likelihoods, 2010.
- [56] N. J. Cornish. Heterodyned likelihood for rapid gravitational wave parameter inference. *Physical Review D*, 104(10), nov 2021.
- [57] R. Cotesta, A. Buonanno, A. Bohé, A. Taracchini, I. Hinder, and S. Ossokine. Enriching the Symphony of Gravitational Waves from Binary Black Holes by Tuning Higher Harmonics. *Phys. Rev. D*, 98(8):084028, 2018.
- [58] D. Coulter, R. Foley, C. Kilpatrick, M. Drout, A. Piro, B. Shappee, M. Siebert, J. Simon, N. Ulloa, D. Kasen, et al. Swope supernova survey 2017a (sss17a), the optical counterpart to a gravitational wave source. *Science*, 358(6370):1556–1558, 2017.
- [59] P. Cowperthwaite, E. Berger, V. Villar, B. Metzger, M. Nicholl, R. Chornock, P. Blanchard, W. f. Fong, R. Margutti, M. Soares-Santos, et al. The electromagnetic counterpart of the binary neutron star merger ligo/virgo gw170817. ii. uv, optical, and near-infrared light curves and comparison to kilonova models. *The Astrophysical Journal Letters*, 848(2):L17, 2017.
- [60] T. Damour. Coalescence of two spinning black holes: An effective one-body approach. *Phys. Rev. D*, 64:124013, Nov 2001.

-
- [61] M. Dax, S. R. Green, J. Gair, J. H. Macke, A. Buonanno, and B. Schölkopf. Real-time gravitational wave science with neural posterior estimation. *Phys. Rev. Lett.*, 127:241103, Dec 2021.
- [62] V. Delfavero. Assessing the convergence of iterative parameter estimation. 2019.
- [63] V. Delfavero, R. O’Shaughnessy, D. Wysocki, and A. Yelikar. Normal approximate likelihoods to gravitational wave events. 2021.
- [64] V. Delfavero, R. O’Shaughnessy, D. Wysocki, and A. Yelikar. Compressed parametric and non-parametric approximations to the gravitational wave likelihood. 2022.
- [65] T. Dietrich, S. Bernuzzi, and W. Tichy. Closed-form tidal approximants for binary neutron star gravitational waveforms constructed from high-resolution numerical relativity simulations. *Phys. Rev. D*, 96(12):121501, 2017.
- [66] T. Dietrich, A. Samajdar, S. Khan, N. K. Johnson-McDaniel, R. Dudi, and W. Tichy. Improving the NRTidal model for binary neutron star systems. *Phys. Rev. D*, 100(4):044003, 2019.
- [67] M. Dominik, K. Belczynski, C. Fryer, D. E. Holz, E. Berti, T. Bulik, I. Mandel, and R. O’Shaughnessy. Double Compact Objects. I. The Significance of the Common Envelope on Merger Rates. *Astrophysical Journal*, 759:52, Nov. 2012.
- [68] M. Dominik, K. Belczynski, C. Fryer, D. E. Holz, E. Berti, T. Bulik, I. Mandel, and R. O’Shaughnessy. Double compact objects. ii. cosmological merger rates. *The Astrophysical Journal*, 779(1):72, 2013.
- [69] M. Dominik, E. Berti, R. O’Shaughnessy, I. Mandel, K. Belczynski, C. Fryer, D. E. Holz, T. Bulik, and F. Pannarale. Double compact objects. iii. gravitational-wave detection rates. *The Astrophysical Journal*, 806(2):263, 2015.
- [70] G. Duchêne and A. Kraus. Stellar Multiplicity. *ARA&A*, 51(1):269–310, Aug. 2013.
- [71] B. Edelman, F. J. Rivera-Paleo, J. D. Merritt, B. Farr, and et al. Constraining unmodeled physics with compact binary mergers from gwtc-1. *Phys. Rev. D*, 103:042004, Feb 2021.
- [72] J. J. Eldridge, E. R. Stanway, L. Xiao, L. A. S. McClelland, G. Taylor, M. Ng, S. M. L. Greis, and J. C. Bray. Binary population and spectral synthesis version 2.1: Construction, observational verification, and new results. *Publications of the Astronomical Society of Australia*, 34:e058, 2017.
- [73] A. Fontana, S. Salimbeni, A. Grazian, E. Giallongo, L. Pentericci, M. Nonino, F. Fontanot, N. Menci, P. Monaco, S. Cristiani, et al. The galaxy mass function up to z in the goods-music sample: into the epoch of formation of massive galaxies. *Astronomy & Astrophysics*, 459(3):745–757, 2006.
- [74] D. Foreman-Mackey, D. W. Hogg, D. Lang, and J. Goodman. emcee: the mcmc hammer. *Publications of the Astronomical Society of the Pacific*, 125(925):306, 2013.

-
- [75] T. Fragos, J. J. Andrews, S. S. Bavera, C. P. L. Berry, S. Coughlin, A. Dotter, P. Giri, V. Kalogera, A. Katsaggelos, K. Kovelakas, S. Lalvani, D. Misra, P. M. Srivastava, Y. Qin, K. A. Rocha, J. Roman-Garza, J. G. Serra, P. Stahle, M. Sun, X. Teng, G. Trajcevski, N. H. Tran, Z. Xing, E. Zapartas, and M. Zevin. Posydon: A general-purpose population synthesis code with detailed binary-evolution simulations, 2022.
- [76] P. Fritschel, L. S. Collaboration, et al. Instrument science white paper 2020. *Technical Report LIGO-T2000407-v3*, 2020.
- [77] C. L. Fryer, K. Belczynski, G. Wiktorowicz, M. Dominik, V. Kalogera, and D. E. Holz. COMPACT REMNANT MASS FUNCTION: DEPENDENCE ON THE EXPLOSION MECHANISM AND METALLICITY. *The Astrophysical Journal*, 749(1):91, mar 2012.
- [78] C. L. Fryer, S. E. Woosley, and D. H. Hartmann. Formation Rates of Black Hole Accretion Disk Gamma-Ray Bursts. *Astrophysical Journal*, 526(1):152–177, Nov. 1999.
- [79] J. Fuller and L. Ma. Most Black Holes Are Born Very Slowly Rotating. *Astrophysical Journal*, 881(1):L1, Aug. 2019.
- [80] J. Fuller, A. L. Piro, and A. S. Jermyn. Slowing the spins of stellar cores. *MNRAS*, 485(3):3661–3680, May 2019.
- [81] R. Gamba, M. Breschi, G. Carullo, P. Rettengo, S. Albanesi, S. Bernuzzi, and A. Nagar. GW190521: A dynamical capture of two black holes. 6 2021.
- [82] C. García-Quirós, M. Colleoni, S. Husa, H. Estellés, G. Pratten, A. Ramos-Buades, M. Mateu-Lucena, and R. Jaume. Multimode frequency-domain model for the gravitational wave signal from nonprecessing black-hole binaries. *Phys. Rev. D*, 102(6):064002, 2020.
- [83] V. Gayathri, J. Healy, J. Lange, B. O’Brien, M. Szczepanczyk, I. Bartos, M. Campanelli, S. Klimentenko, C. Lousto, and R. O’Shaughnessy. Eccentricity estimate for black hole mergers with numerical relativity simulations. *Nature Astronomy*, 6:344–349, mar 2022.
- [84] S. Ghosh, X. Liu, J. Creighton, I. M. n. Hernandez, W. Kastaun, and G. Pratten. Rapid model comparison of equations of state from gravitational wave observation of binary neutron star coalescences. *Phys. Rev. D*, 104:083003, Oct 2021.
- [85] N. Giacobbo, M. Mapelli, and M. Spera. Merging black hole binaries: the effects of progenitor’s metallicity, mass-loss rate and Eddington factor. *Monthly Notices of the Royal Astronomical Society*, 474(3):2959–2974, 11 2017.
- [86] J. Golomb and C. Talbot. Hierarchical inference of binary neutron star mass distribution and equation of state with gravitational waves. *The Astrophysical Journal*, 926(1):79, feb 2022.
- [87] A. Gualandris, M. Colpi, S. P. Zwart, and A. Possenti. Has the black hole in XTE j1118+480 experienced an asymmetric natal kick? *The Astrophysical Journal*, 618(2):845–851, jan 2005.

-
- [88] J. E. Gunn and J. P. Ostriker. On the Nature of Pulsars. III. Analysis of Observations. *Astrophysical Journal*, 160:979, June 1970.
- [89] I. Hachisu, M. Kato, K. Nomoto, and H. Umeda. A new evolutionary path to type ia supernovae: A helium-rich supersoft x-ray source channel. *The Astrophysical Journal*, 519(1):314–323, jul 1999.
- [90] W. R. Hamann, L. Koesterke, and U. Wessolowski. Spectral analyses of the Galactic Wolf-Rayet stars: hydrogen-helium abundances and improved stellar parameters for the WN class. *A&A*, 299:151, July 1995.
- [91] M. Hannam, P. Schmidt, A. Bohé, L. Haegel, S. Husa, F. Ohme, G. Pratten, and M. Pürrer. Simple Model of Complete Precessing Black-Hole-Binary Gravitational Waveforms. *Phys. Rev. Lett.*, 113(15):151101, 2014.
- [92] W. K. Hastings. Monte carlo sampling methods using markov chains and their applications. 1970.
- [93] J. Healy, C. O. Lousto, J. Lange, and R. O’Shaughnessy. Application of the third RIT binary black hole simulations catalog to parameter estimation of gravitational-wave signals from the LIGO-Virgo O1 and O2 observational runs. *Phys. Rev. D*, 102(12):124053, Dec. 2020.
- [94] I. Hinder, A. Buonanno, M. Boyle, and Z. B. E. et al. Error-analysis and comparison to analytical models of numerical waveforms produced by the NRAR collaboration. *Classical and Quantum Gravity*, 31(2):025012, jan 2013.
- [95] T. Hinderer et al. Effects of neutron-star dynamic tides on gravitational waveforms within the effective-one-body approach. *Phys. Rev. Lett.*, 116(18):181101, 2016.
- [96] G. Hobbs, D. R. Lorimer, A. G. Lyne, and M. Kramer. A statistical study of 233 pulsar proper motions. *Monthly Notices of the Royal Astronomical Society*, 360(3):974–992, 07 2005.
- [97] E. M. Holmbeck, R. O’Shaughnessy, V. Delfavero, and K. Belczynski. A nuclear equation of state inferred from stellar r-process abundances. *The Astrophysical Journal*, 926(2):196, feb 2022.
- [98] Y. Huang, C.-J. Haster, J. Roulet, S. Vitale, and et al. Source properties of the lowest signal-to-noise-ratio binary black hole detections. *Phys. Rev. D*, 102(10):103024, Nov. 2020.
- [99] J. R. Hurley, O. R. Pols, and C. A. Tout. Comprehensive analytic formulae for stellar evolution as a function of mass and metallicity. *Monthly Notices of the Royal Astronomical Society*, 315(3):543–569, 07 2000.
- [100] J. R. Hurley, C. A. Tout, and O. R. Pols. Evolution of binary stars and the effect of tides on binary populations. *Monthly Notices of the Royal Astronomical Society*, 329(4):897–928, 02 2002.

-
- [101] S. Husa, S. Khan, M. Hannam, M. Pürrer, F. Ohme, X. J. Forteza, and A. Bohé. Frequency-domain gravitational waves from nonprecessing black-hole binaries. i. new numerical waveforms and anatomy of the signal. *Phys. Rev. D*, 93:044006, Feb 2016.
- [102] S. Husa, S. Khan, M. Hannam, M. Pürrer, F. Ohme, X. Jiménez Forteza, and A. Bohé. Frequency-domain gravitational waves from nonprecessing black-hole binaries. I. New numerical waveforms and anatomy of the signal. *Phys. Rev. D*, 93(4):044006, 2016.
- [103] N. Ivanova. COMMON ENVELOPE: ON THE MASS AND THE FATE OF THE REMNANT. *The Astrophysical Journal*, 730(2):76, mar 2011.
- [104] N. Ivanova and S. Chaichenets. COMMON ENVELOPE: ENTHALPY CONSIDERATION. *The Astrophysical Journal*, 731(2):L36, mar 2011.
- [105] R. G. Izzard, C. A. Tout, A. I. Karakas, and O. R. Pols. A new synthetic model for asymptotic giant branch stars. *Monthly Notices of the Royal Astronomical Society*, 350(2):407–426, 05 2004.
- [106] Izzard, R. G., Dray, L. M., Karakas, A. I., Lugaro, M., and Tout, C. A. Population nucleosynthesis in single and binary stars - i. model. *A&A*, 460(2):565–572, 2006.
- [107] Izzard, R. G., Glebbeek, E., Stancliffe, R. J., and Pols, O. R. Population synthesis of binary carbon-enhanced metal-poor stars*. *A&A*, 508(3):1359–1374, 2009.
- [108] K. Jani, J. Healy, J. A. Clark, L. London, P. Laguna, and D. Shoemaker. Georgia tech catalog of gravitational waveforms. *Classical and Quantum Gravity*, 33(20):204001, sep 2016.
- [109] P. Jaranowski and A. Królak. Gravitational-wave data analysis. formalism and sample applications: The gaussian case, 2007.
- [110] D. Kasen, B. Metzger, J. Barnes, E. Quataert, and E. Ramirez-Ruiz. Origin of the heavy elements in binary neutron-star mergers from a gravitational-wave event. *Nature*, 551(7678):80–84, 2017.
- [111] S. Khan, K. Chatziioannou, M. Hannam, and F. Ohme. Phenomenological model for the gravitational-wave signal from precessing binary black holes with two-spin effects. *Physical Review D*, 100(2), jul 2019.
- [112] S. Khan, S. Husa, M. Hannam, F. Ohme, M. Pürrer, X. J. Forteza, and A. Bohé. Frequency-domain gravitational waves from nonprecessing black-hole binaries. ii. a phenomenological model for the advanced detector era. *Phys. Rev. D*, 93:044007, Feb 2016.
- [113] S. Khan, F. Ohme, K. Chatziioannou, and M. Hannam. Including higher order multipoles in gravitational-wave models for precessing binary black holes. *Phys. Rev. D*, 101(2):024056, 2020.
- [114] C. D. Kilpatrick, R. J. Foley, D. Kasen, A. Murguia-Berthier, E. Ramirez-Ruiz, D. A. Coulter, M. R. Drout, A. L. Piro, B. J. Shappee, K. Boutsia, et al. Electromagnetic evidence that sss17a is the result of a binary neutron star merger. *Science*, 358(6370):1583–1587, 2017.

-
- [115] R. Kippenhahn and A. Weigert. *Stellar Structure and Evolution*. Springer-Verlag, 1994.
- [116] S. Kirkpatrick, C. D. Gelatt, and M. P. Vecchi. Optimization by simulated annealing. *Science*, 220(4598):671–680, 1983.
- [117] J. Klencki, M. Moe, W. Gladysz, M. Chruslinska, D. E. Holz, and K. Belczynski. Impact of inter-correlated initial binary parameters on double black hole and neutron star mergers. *A&A*, 619:A77, Nov. 2018.
- [118] J. Klencki, G. Nelemans, A. G. Istrate, and M. Chruslinska. It has to be cool: Supergiant progenitors of binary black hole mergers from common-envelope evolution. *Astronomy & Astrophysics*, 645:A54, Jan 2021.
- [119] H. A. Kobulnicky and C. L. Fryer. A new look at the binary characteristics of massive stars. *The Astrophysical Journal*, 670(1):747, 2007.
- [120] B. Kocsis and J. Levin. Repeated bursts from relativistic scattering of compact objects in galactic nuclei. *Phys. Rev. D*, 85:123005, Jun 2012.
- [121] A. Kolmogorov. Sulla determinazione empirica di una legge di distribuzione. *Inst. Ital. Attuari, Giorn.*, 4:83–91, 1933.
- [122] P. Kroupa, C. A. Tout, and G. Gilmore. The distribution of low-mass stars in the Galactic disc. *Monthly Notices of the Royal Astronomical Society*, 262(3):545–587, 06 1993.
- [123] P. Kroupa and C. Weidner. Galactic-field initial mass functions of massive stars. *The Astrophysical Journal*, 598(2):1076–1078, dec 2003.
- [124] M. U. Kruckow, T. M. Tauris, N. Langer, M. Kramer, and R. G. Izzard. Progenitors of gravitational wave mergers: binary evolution with the stellar grid-based code ComBinE. *Monthly Notices of the Royal Astronomical Society*, 481(2):1908–1949, 08 2018.
- [125] J. Lange, R. O’Shaughnessy, and M. Rizzo. Rapid and accurate parameter inference for coalescing, precessing compact binaries, 2018.
- [126] N. Leslie, L. Dai, and G. Pratten. Mode-by-mode relative binning: Fast likelihood estimation for gravitational waveforms with spin-orbit precession and multiple harmonics. *Physical Review D*, 104(12), dec 2021.
- [127] S.-C. Leung, K. Nomoto, and S. Blinnikov. Pulsational Pair-instability Supernovae. I. Precollapse Evolution and Pulsational Mass Ejection. *Astrophysical Journal*, 887(1):72, Dec. 2019.
- [128] V. M. Lipunov, K. A. Postnov, M. E. Prokhorov, and A. I. Bogomazov. Description of the “Scenario Machine”. *Astronomy Reports*, 53(10):915–940, Oct. 2009.
- [129] M. Livio and N. Soker. The Common Envelope Phase in the Evolution of Binary Stars. *Astrophysical Journal*, 329:764, June 1988.

-
- [130] F. Löffler, J. Faber, E. Bentivegna, T. Bode, P. Diener, R. Haas, I. Hinder, B. C. Mundim, C. D. Ott, E. Schnetter, G. Allen, M. Campanelli, and P. Laguna. The einstein toolkit: a community computational infrastructure for relativistic astrophysics. *Classical and Quantum Gravity*, 29(11):115001, may 2012.
- [131] L. Ma and J. Fuller. Angular momentum transport in massive stars and natal neutron star rotation rates. *MNRAS*, 488(3):4338–4355, Sept. 2019.
- [132] P. Madau and T. Fragos. Radiation backgrounds at cosmic dawn: X-rays from compact binaries. *The Astrophysical Journal*, 840(1):39, may 2017.
- [133] G. Meynet, V. Chomienne, S. Ekström, C. Georgy, A. Granada, J. Groh, A. Maeder, P. Eggenberger, E. Levesque, and P. Massey. Impact of mass-loss on the evolution and pre-supernova properties of red supergiants. *A&A*, 575:A60, Mar. 2015.
- [134] M. C. Miller and D. P. Hamilton. Four-body effects in globular cluster black hole coalescence. *The Astrophysical Journal*, 576(2):894–898, sep 2002.
- [135] M. M. Moreno, F. R. N. Schneider, F. K. Roepke, S. T. Ohlmann, R. Pakmor, P. Podsiadlowski, and C. Sand. From 3D hydrodynamic simulations of common-envelope interaction to gravitational-wave mergers. *arXiv e-prints*, page arXiv:2111.12112, Nov. 2021.
- [136] M. Morscher, B. Pattabiraman, C. Rodriguez, F. A. Rasio, and S. Umbreit. THE DYNAMICAL EVOLUTION OF STELLAR BLACK HOLES IN GLOBULAR CLUSTERS. *The Astrophysical Journal*, 800(1):9, feb 2015.
- [137] A. H. Mroué, M. A. Scheel, B. Szilágyi, H. P. Pfeiffer, M. Boyle, D. A. Hemberger, L. E. Kidder, G. Lovelace, S. Ossokine, N. W. Taylor, A. Zenginoğlu, L. T. Buchman, T. Chu, E. Foley, M. Giesler, R. Owen, and S. A. Teukolsky. Catalog of 174 binary black hole simulations for gravitational wave astronomy. *Physical Review Letters*, 111(24), dec 2013.
- [138] A. Nagar et al. Time-domain effective-one-body gravitational waveforms for coalescing compact binaries with nonprecessing spins, tides and self-spin effects. *Phys. Rev. D*, 98(10):104052, 2018.
- [139] S. Naoz, B. Kocsis, A. Loeb, and N. Yunes. RESONANT POST-NEWTONIAN ECCENTRICITY EXCITATION IN HIERARCHICAL THREE-BODY SYSTEMS. *The Astrophysical Journal*, 773(2):187, aug 2013.
- [140] R. Narayan, T. Piran, and A. Shemi. Neutron Star and Black Hole Binaries in the Galaxy. 379:L17, Sept. 1991.
- [141] H. Nieuwenhuijzen and C. de Jager. Parametrization of stellar rates of mass loss as functions of the fundamental stellar parameters M, L, and R. *A&A*, 231:134–136, May 1990.

-
- [142] A. H. Nitz, C. D. Capano, S. Kumar, Y.-F. Wang, S. Kastha, M. Schäfer, R. Dhurkunde, and M. Cabero. 3-OGC: Catalog of gravitational waves from compact-binary mergers. *The Astrophysical Journal*, 922(1):76, nov 2021.
- [143] J. Nordhaus, T. D. Brandt, A. Burrows, and A. Almgren. The hydrodynamic origin of neutron star kicks. *Monthly Notices of the Royal Astronomical Society*, 423(2):1805–1812, 06 2012.
- [144] J. Nordhaus, T. D. Brandt, A. Burrows, E. Livne, and C. D. Ott. Theoretical support for the hydrodynamic mechanism of pulsar kicks. *Phys. Rev. D*, 82(10):103016, Nov. 2010.
- [145] R. M. O’Leary, B. Kocsis, and A. Loeb. Gravitational waves from scattering of stellar-mass black holes in galactic nuclei. *Monthly Notices of the Royal Astronomical Society*, 395(4):2127–2146, 05 2009.
- [146] R. O’Shaughnessy, B. Farr, E. Ochsner, H.-S. Cho, C. Kim, and C.-H. Lee. Parameter estimation of gravitational waves from nonprecessing black hole-neutron star inspirals with higher harmonics: Comparing Markov-chain Monte Carlo posteriors to an effective Fisher matrix. *Phys. Rev. D*, 89(6):064048, Mar. 2014.
- [147] R. O’Shaughnessy, B. Farr, E. Ochsner, H.-S. Cho, V. Raymond, C. Kim, and C.-H. Lee. Parameter estimation of gravitational waves from precessing black hole-neutron star inspirals with higher harmonics. *Phys. Rev. D*, 89:102005, May 2014.
- [148] L. M. Oskinova, H. Todt, R. Ignace, J. C. Brown, J. P. Cassinelli, and W. R. Hamann. Early magnetic B-type stars: X-ray emission and wind properties. *MNRAS*, 416(2):1456–1474, Sept. 2011.
- [149] S. Ossokine, A. Buonanno, S. Marsat, R. Cotesta, S. Babak, T. Dietrich, R. Haas, I. Hinder, H. P. Pfeiffer, M. Pürrer, C. J. Woodford, M. Boyle, L. E. Kidder, M. A. Scheel, and B. Szilágyi. Multipolar effective-one-body waveforms for precessing binary black holes: Construction and validation. *Physical Review D*, 102(4), aug 2020.
- [150] S. Ossokine et al. Multipolar Effective-One-Body Waveforms for Precessing Binary Black Holes: Construction and Validation. *Phys. Rev. D*, 102(4):044055, 2020.
- [151] R. O’Shaughnessy, D. Gerosa, and D. Wysocki. Inferences about supernova physics from gravitational-wave measurements: Gw151226 spin misalignment as an indicator of strong black-hole natal kicks. *Physical Review Letters*, 119(1), Jul 2017.
- [152] R. O’Shaughnessy, V. Kalogera, and K. Belczynski. Binary compact object coalescence rates: The role of elliptical galaxies. *The Astrophysical Journal*, 716(1):615–633, May 2010.
- [153] B. Paczynski. Common Envelope Binaries. In P. Eggleton, S. Mitton, and J. Whelan, editors, *Structure and Evolution of Close Binary Systems*, volume 73, page 75, Jan. 1976.

-
- [154] Y. Pan, A. Buonanno, A. Taracchini, L. E. Kidder, A. H. Mroué, H. P. Pfeiffer, M. A. Scheel, and B. Szilágyi. Inspiral-merger-ringdown waveforms of spinning, precessing black-hole binaries in the effective-one-body formalism. *Phys. Rev. D*, 89(8):084006, 2014.
- [155] C. Pankow, P. Brady, E. Ochsner, and R. O’Shaughnessy. Novel scheme for rapid parallel parameter estimation of gravitational waves from compact binary coalescences. *Phys. Rev. D*, 92:023002, Jul 2015.
- [156] F. Pedregosa, G. Varoquaux, A. Gramfort, V. Michel, B. Thirion, O. Grisel, M. Blondel, P. Prettenhofer, R. Weiss, V. Dubourg, J. Vanderplas, A. Passos, D. Cournapeau, M. Brucher, M. Perrot, and E. Duchesnay. Scikit-learn: Machine learning in Python. *Journal of Machine Learning Research*, 12:2825–2830, 2011.
- [157] P. Podsiadlowski, P. C. Joss, and J. J. L. Hsu. Presupernova Evolution in Massive Interacting Binaries. *Astrophysical Journal*, 391:246, May 1992.
- [158] E. Poisson and C. M. Will. Gravitational waves from inspiraling compact binaries: Parameter estimation using second-post-Newtonian waveforms. *Phys. Rev. D*, 52:848–855, July 1995.
- [159] S. F. Portegies Zwart. The formation of Be stars in close binary systems. The importance of kicks and angular-momentum loss. *A&A*, 296:691, Apr. 1995.
- [160] S. F. Portegies Zwart and L. R. Yungelson. Formation and evolution of binary neutron stars. *A&A*, 332:173–188, Apr. 1998.
- [161] J. Poutanen, A. Veledina, A. V. Berdyugin, S. V. Berdyugina, H. Jermak, P. G. Jonker, J. J. E. Kajava, I. A. Kosenkov, V. Kravtsov, V. Piirola, M. Shrestha, M. A. P. Torres, and S. S. Tsygankov. Black hole spin–orbit misalignment in the x-ray binary maxi j1820+070. *Science*, 375(6583):874–876, 2022.
- [162] G. Pratten, C. Garcí a-Quirós, M. Colleoni, A. Ramos-Buades, H. Estellés, M. Mateu-Lucena, R. Jaume, M. Haney, D. Keitel, J. E. Thompson, and S. Husa. Computationally efficient models for the dominant and subdominant harmonic modes of precessing binary black holes. *Physical Review D*, 103(10), may 2021.
- [163] G. Pratten, S. Husa, C. Garcia-Quiros, M. Colleoni, A. Ramos-Buades, H. Estelles, and R. Jaume. Setting the cornerstone for a family of models for gravitational waves from compact binaries: The dominant harmonic for nonprecessing quasicircular black holes. *Phys. Rev. D*, 102(6):064001, 2020.
- [164] E. Racine, A. Buonanno, and L. Kidder. Recoil velocity at second post-newtonian order for spinning black hole binaries. *Phys. Rev. D*, 80:044010, Aug 2009.
- [165] V. Ramachandran, W. R. Hamann, L. M. Oskinova, J. S. Gallagher, R. Hainich, T. Shenar, A. A. C. Sander, H. Todt, and L. Fulmer. Testing massive star evolution, star formation history,

-
- and feedback at low metallicity. Spectroscopic analysis of OB stars in the SMC Wing. *A&A*, 625:A104, May 2019.
- [166] A. Ramos-Buades, S. Husa, G. Pratten, H. Estellés, C. García-Quirós, M. Mateu-Lucena, M. Colleoni, and R. Jaume. First survey of spinning eccentric black hole mergers: Numerical relativity simulations, hybrid waveforms, and parameter estimation. *Phys. Rev. D*, 101:083015, Apr 2020.
- [167] S. Rappaport, P. C. Joss, and R. F. Webbink. The evolution of highly compact binary stellar systems. *Astrophysical Journal*, 254:616–640, Mar. 1982.
- [168] S. Rappaport, F. Verbunt, and P. C. Joss. A new technique for calculations of binary stellar evolution application to magnetic braking. *Astrophysical Journal*, 275:713–731, Dec. 1983.
- [169] J. Riley, P. Agrawal, J. W. Barrett, K. N. K. Boyett, F. S. Broekgaarden, D. Chattopadhyay, S. M. Gaebel, F. Gittins, R. Hirai, G. Howitt, S. Justham, L. Khandelwal, F. Kummer, M. Y. M. Lau, I. Mandel, S. E. de Mink, C. Neijssel, T. Riley, L. van Son, S. Stevenson, A. Vigna-Gómez, S. Vinciguerra, T. Wagg, and R. Willcox. Rapid stellar and binary population synthesis with compas. *The Astrophysical Journal Supplement Series*, 258(2):34, Feb 2022.
- [170] I. Romero-Shaw, P. D. Lasky, E. Thrane, and J. C. Bustillo. GW190521: Orbital eccentricity and signatures of dynamical formation in a binary black hole merger signal. *The Astrophysical Journal*, 903(1):L5, oct 2020.
- [171] J. Sadiq, T. Dent, and D. Wysocki. Flexible and fast estimation of binary merger population distributions with adaptive kde, 2021.
- [172] E. E. Salpeter. The Luminosity Function and Stellar Evolution. *Astrophysical Journal*, 121:161, Jan. 1955.
- [173] J. D. Scargle, J. P. Norris, B. Jackson, and J. Chiang. Studies in Astronomical Time Series Analysis. VI. Bayesian Block Representations. *Astrophysical Journal*, 764(2):167, Feb. 2013.
- [174] P. Schechter. An analytic expression for the luminosity function for galaxies. *Astrophysical Journal*, 203:297–306, Jan. 1976.
- [175] B. Shappee, J. Simon, M. Drout, A. Piro, N. Morrell, J. Prieto, D. Kasen, T.-S. Holoiien, J. Kollmeier, D. Kelson, et al. Early spectra of the gravitational wave source gw170817: evolution of a neutron star merger. *Science*, 358(6370):1574–1578, 2017.
- [176] M. Shikauchi, A. Tanikawa, and N. Kawanaka. Detectability of black hole binaries with gaia: Dependence on binary evolution models, 2022.
- [177] K. Silsbee and S. Tremaine. Lidov-Kozai Cycles with Gravitational Radiation: Merging Black Holes in Isolated Triple Systems. *Astrophysical Journal*, 836(1):39, Feb. 2017.

-
- [178] L. P. Singer and L. R. Price. Rapid bayesian position reconstruction for gravitational-wave transients. *Physical Review D*, 93(2), jan 2016.
- [179] M. Spera, M. Mapelli, and A. Bressan. The mass spectrum of compact remnants from the parsec stellar evolution tracks. *Monthly Notices of the Royal Astronomical Society*, 451(4):4086–4103, 06 2015.
- [180] J. Steinhoff, T. Hinderer, A. Buonanno, and A. Taracchini. Dynamical Tides in General Relativity: Effective Action and Effective-One-Body Hamiltonian. *Phys. Rev. D*, 94(10):104028, 2016.
- [181] S. Stevenson, A. Vigna-Gómez, I. Mandel, J. W. Barrett, C. J. Neijssel, D. Perkins, and S. E. de Mink. Formation of the first three gravitational-wave observations through isolated binary evolution. *Nature Communications*, 8(1), Apr 2017.
- [182] C. Talbot, R. Smith, E. Thrane, and G. B. Poole. Parallelized inference for gravitational-wave astronomy. *Phys. Rev. D*, 100:043030, Aug 2019.
- [183] A. Taracchini et al. Effective-one-body model for black-hole binaries with generic mass ratios and spins. *Phys. Rev. D*, 89(6):061502, 2014.
- [184] T. M. Tauris and M. Bailes. The origin of millisecond pulsar velocities. *A&A*, 315:432–444, Nov. 1996.
- [185] The LIGO Scientific Collaboration. GW190412: Observation of a binary-black-hole coalescence with asymmetric masses. *Physical Review D*, 102(4), aug 2020.
- [186] The LIGO Scientific Collaboration, B. P. Abbott, R. Abbott, and T. D. Abbott. Prospects for observing and localizing gravitational-wave transients with advanced LIGO, advanced virgo and KAGRA. *Living Reviews in Relativity*, 23(1), sep 2020.
- [187] The LIGO Scientific Collaboration, R. Abbott, T. D. Abbott, S. Abraham, and F. Acernese. GW190814: Gravitational waves from the coalescence of a 23 solar mass black hole with a 2.6 solar mass compact object. *The Astrophysical Journal Letters*, 896(2):L44, jun 2020.
- [188] The LIGO Scientific Collaboration, the Virgo Collaboration, B. P. Abbott, R. Abbott, T. D. Abbott, S. Abraham, and et al. Population properties of compact objects from the second LIGO–Virgo Gravitational-Wave Transient Catalog. *Available as LIGO-P2000077*, Oct. 2020.
- [189] V. Tiwari. VAMANA: modeling binary black hole population with minimal assumptions. *Classical and Quantum Gravity*, 38(15):155007, jul 2021.
- [190] S. Toonen, A. Hamers, and S. P. Zwart. The evolution of hierarchical triple star-systems, 2016.
- [191] Toonen, S., Nelemans, G., and Portegies Zwart, S. Supernova type ia progenitors from merging double white dwarfs - using a new population synthesis model. *A&A*, 546:A70, 2012.

-
- [192] A. Tutukov and L. Yungelson. Close binary stars: Observations and interpretation statistical investigation of spectroscopic binary stars. *Proceedings of the International Astronomical Union*, 88:15–22, 01 1980.
- [193] D. Vanbeveren, E. De Donder, J. Van Bever, W. Van Rensbergen, and C. De Loore. The wr and o-type star population predicted by massive star evolutionary synthesis. *New Astronomy*, 3(7):443–492, 1998.
- [194] D. Vanbeveren, C. De Loore, and W. Van Rensbergen. Massive stars. *aapr*, 9(1-2):63–152, Jan. 1998.
- [195] V. Varma, S. E. Field, M. A. Scheel, J. Blackman, D. Gerosa, L. C. Stein, L. E. Kidder, and H. P. Pfeiffer. Surrogate models for precessing binary black hole simulations with unequal masses. *Physical Review Research*, 1(3), oct 2019.
- [196] J. Veitch, V. Raymond, B. Farr, W. Farr, P. Graff, S. Vitale, B. Aylott, K. Blackburn, N. Christensen, M. Coughlin, W. Del Pozzo, F. Feroz, J. Gair, C.-J. Haster, V. Kalogera, T. Littenberg, I. Mandel, R. O’Shaughnessy, M. Pitkin, C. Rodriguez, C. Röver, T. Sidery, R. Smith, M. Van Der Sluys, A. Vecchio, W. Voudsen, and L. Wade. Parameter estimation for compact binaries with ground-based gravitational-wave observations using the lalinference software library. *Phys. Rev. D*, 91:042003, Feb 2015.
- [197] J. S. Vink, A. de Koter, and H. J. G. L. M. Lamers. Mass-loss predictions for O and B stars as a function of metallicity. *A&A*, 369:574–588, Apr. 2001.
- [198] S. Vitale, D. Gerosa, C.-J. Haster, K. Chatziioannou, and A. Zimmerman. Impact of Bayesian Priors on the Characterization of Binary Black Hole Coalescences. *Phys. Rev. Lett.*, 119(25):251103, 2017.
- [199] L. Wade, J. D. E. Creighton, E. Ochsner, B. D. Lackey, B. F. Farr, T. B. Littenberg, and V. Raymond. Systematic and statistical errors in a bayesian approach to the estimation of the neutron-star equation of state using advanced gravitational wave detectors. *Phys. Rev. D*, 89:103012, May 2014.
- [200] C. Wang, K. Jia, and X.-D. Li. The binding energy parameter for common envelope evolution. *Research in Astronomy and Astrophysics*, 16(8):009, aug 2016.
- [201] C. K. Williams and C. E. Rasmussen. *Gaussian processes for machine learning*, volume 2. MIT press Cambridge, MA, 2006.
- [202] E. B. Wilson. Probable inference, the law of succession, and statistical inference. *Journal of the American Statistical Association*, 22(158):209–212, 1927.
- [203] E. C. Wilson and J. Nordhaus. Convection Reconciles the Difference in Efficiencies Between Low-Mass and High-Mass Common Envelopes. *arXiv e-prints*, page arXiv:2203.06091, Mar. 2022.

-
- [204] J. Wofford, A. Yelikar, H. Gallagher, E. Champion, D. Wysocki, V. Delfavero, J. Lange, C. Rose, S. Morisaki, and R. O’Shaughnessy. Expanding rift: Improving performance for gw parameter inference. 2022.
- [205] A. Wongwathanarat, H.-T. Janka, and E. Müller. Hydrodynamical neutron star kicks in three dimensions. *The Astrophysical Journal*, 725, 2010.
- [206] S. E. Woosley, A. Heger, and T. A. Weaver. The evolution and explosion of massive stars. *Rev. Mod. Phys.*, 74:1015–1071, Nov 2002.
- [207] D. Wysocki, D. Gerosa, R. O’Shaughnessy, K. Belczynski, W. Gladysz, E. Berti, M. Kesden, and D. E. Holz. Explaining ligo’s observations via isolated binary evolution with natal kicks. *Physical Review D*, 97(4), Feb 2018.
- [208] D. Wysocki, J. Lange, and R. O’Shaughnessy. Reconstructing phenomenological distributions of compact binaries via gravitational wave observations. *Physical Review D*, 100(4), Aug 2019.
- [209] X.-J. Xu and X.-D. Li. ON THE BINDING ENERGY PARAMETER λ OF COMMON ENVELOPE EVOLUTION. *The Astrophysical Journal*, 716(1):114–121, may 2010.
- [210] B. Zackay, L. Dai, and T. Venumadhav. Relative binning and fast likelihood evaluation for gravitational wave parameter estimation, 2018.
- [211] M. ZILHÁ O and F. LÖFFLER. AN INTRODUCTION TO THE EINSTEIN TOOLKIT. *International Journal of Modern Physics A*, 28(22n23):1340014, sep 2013.
- [212] S. F. P. Zwart, H. Baumgardt, P. Hut, J. Makino, and S. L. W. McMillan. Formation of massive black holes through runaway collisions in dense young star clusters. *Nature*, 428(6984):724–726, apr 2004.
- [213] S. F. P. Zwart and S. L. W. McMillan. The runaway growth of intermediate-mass black holes in dense star clusters. *The Astrophysical Journal*, 576(2):899–907, sep 2002.